Modelling soft-tissue motion during human movement experiments to improve calculations of skeletal kinematics

Firas Baklouti

Supervised by Dr. Thomas Uchida

A thesis submitted in partial fulfillment of the requirements for the
Master's degree in Biomedical Engineering

Ottawa–Carleton Institute for Biomedical Engineering
Faculty of Engineering
University of Ottawa

© Firas Baklouti, Ottawa, Canada, 2021

Abstract

In Canada, approximately 544,000 upper-limb injuries occurred in a 12-month period between 2009 and 2010, many of which were injuries to the rotator cuff muscles of the shoulder. Because of the complex structure and function of the shoulder, it is often difficult to determine which muscles have been injured. The most widely used technology to study human movement is motion capture, wherein markers are affixed to a subject's skin and are tracked by cameras as the subject moves. The recorded marker trajectories are then used to estimate the bone locations and joint angles during the tracked motion. This is called an *inverse kinematic simulation*. The simulation can then be used to estimate variables that are difficult or impossible to measure directly, such as the activation of single muscle heads within a muscle group. However, muscles bulge and skin stretches during movement, so the markers that are affixed to the skin generally move relative to the underlying bones. These errors, known as soft-tissue artifacts, lead to uncertainty in the calculation of bone locations and, consequently, uncertainty in the computed skeletal joint angles. This uncertainty limits the use of inverse kinematic simulations in clinical settings. Given the skin tissue's elastic behaviour, a spring-based equilibrium model can be used to estimate the behaviour of skin during non-impulsive motion. In the proposed model, markers were placed on the surface of ellipsoids (representing the thorax, abdomen, scapula, and upper arm) and were attached to each other via springs. The system was assumed to remain in static equilibrium during sufficiently slow movements to approximate the stretch of the skin. In this thesis, the development and application of a proof-of-concept model to estimate the pose of the skeleton is described. This work demonstrates the feasibility of using such a model to reduce errors due to soft-tissue motion.

Table of Contents

List of Figures

List of Algorithms

List of Symbols

c	Damping coefficient
F	Force
k	Spring constant
J	Objective function
l	Spring length
l_{slack}	Spring slack length
Δl	Spring stretch ($\Delta l = l - l_{\text{slack}}$)
PE	Potential energy of spring
R	Repulsive force
v	Velocity
x	Displacement

1. Introduction

This chapter explains what movement analysis is and why it is needed, and provides several applications in which human movement analysis is used. The concepts of inverse kinematics, inverse dynamics and forward dynamics are then discussed. Finally, the contributions of this work are summarized and an outline of the remainder of the thesis is provided.

1.1 Movement analysis

Understanding human movement is critical for developing effective prosthetic devices and treatments for musculoskeletal impairments. This knowledge can be used to understand the mechanisms of pathological movements and help in the development of treatments. For example, measuring compensations in the gait of individuals with knee osteoarthritis, such as increased pelvic motion, can be used to monitor disease progression [1]. Additionally, motion analysis can be used to evaluate the effectiveness of a treatment, such as analyzing gait before and after a total knee replacement surgery to measure changes in step length and walking speed [1]. Our understanding of typical gait is also used in the development of orthoses to treat changes in movement due to injury—for example, to correct asymmetric weight bearing that can be observed in stroke patients due to reduced muscle function [1]. Finally, motion analysis can be used to prevent injury and enhance the performance of athletes. For example, analysis of the biomechanics of the elliptical exercise indicates that the increased step length in the exercise could lead to harmful knee joint loading but an increased step height during the exercise can reduce the risk of other injuries [1].

Human movement analysis is performed through direct observation and by using analytical techniques to quantify motion, such as skeletal joint angles and the activity of muscles over time. One fundamental goal is to compute the forces that are responsible for generating an observed movement. The magnitudes of the internal forces generated by muscles and within joints are difficult to obtain through non-invasive experimentation, and thus experimental measurements are used alongside mathematical models to estimate these forces. (Note that the musculoskeletal system is over-actuated—that is, there are more muscles than degrees of freedom—and thus measurement of the body's motion is not sufficient to uniquely compute the force generated by each muscle.) Experimental tools that are used to study human movement can be divided into two categories (see Figure 1.1): invasive techniques, such as fluoroscopy (a continuous X-ray), which directly measure the movement of internal structures; and non-invasive techniques, such as optical motion capture, which typically involves tracking the motion of skin-mounted markers to measure the movement of the body. Optical motion capture is the most commonly used technique for analyzing the movement of patients with neuromusculoskeletal disorders [1].

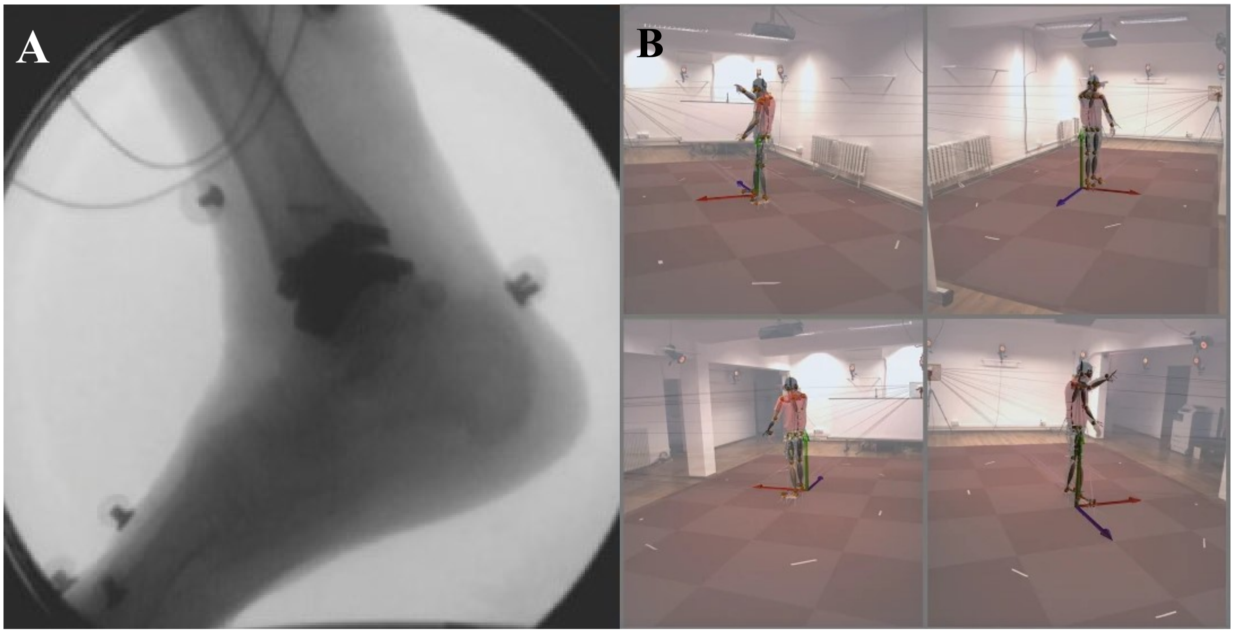

Figure 1.1: Two common strategies for measuring skeletal kinematics. A, image from X-ray fluoroscope; B, optical motion capture. Panel A is reproduced from Blair et al. [2] and is licensed under Creative Commons Attribution License (CC BY). Panel B is reproduced from Malleson et al. [3] and is licensed under Creative Commons Attribution 4.0 International.

A challenge with optical motion capture systems is that the skin-mounted markers move relative to the underlying bones whose motion is being sought. This relative motion occurs because soft tissues deform as humans move: muscles bulge, fat jiggles, and skin stretches. Collectively, these sources of measurement error are referred to as soft-tissue artifacts (STA), which affect the results obtained from movement analysis. Invasive techniques such as bone pins (described in Chapter 2) can provide direct measurements of skeletal motion but can alter an individual's movement; fluoroscopy has a small field of view (and exposes the subject to ionizing radiation) which limits its practical application. The challenges associated with soft-tissue motion are particularly apparent when studying jumping, where a large amount of STA is present during landing but where a large field of view is required [4,5]. An effective method to reduce STA non-invasively would be beneficial in studies that involve movements with large accelerations and that require a large field of view.

1.2 Applications of movement analysis

Prostheses and orthoses

A prosthesis is a device that replicates the function and/or structure of a limb. Developing a prosthesis to replace an amputated lower limb, for example, requires a thorough understanding of the typical gait cycle. This includes understanding the changes in the joint angles during a patient's gait before the amputation, the muscle activity in each stage of the gait cycle, and the strength of the individual. Moreover, the prosthesis should avoid changing the centre of gravity or causing compensatory movements that could increase energy expenditure or introduce asymmetry. Such changes could damage soft tissue in the residual limb or overburden certain muscle groups. Physiological properties of the individual, such as body weight, height and the shape of the residual limb, should also be considered when selecting a prosthesis [6].

An orthosis is a device that is worn on a limb to improve function. Understanding of typical motion allows one to identify and correct pathological movements. For example, the plantar fascia is a band of fibrous tissue located at the bottom of the foot that provides support during walking. A common condition in the foot is plantar fasciitis, wherein the section of the plantar fascia under the heel is damaged, causing pain [7]. A foot orthosis can help redistribute the body's weight and reduce the force being applied to the fascia, thus reducing pain and preventing compensatory movements [8]. Foot orthoses are also used to assist in the treatment of patients who suffer from malalignment syndrome, in which asymmetry is present in the body's posture due to misalignment of bones. This condition can also result in painful atypical gait patterns and asymmetries in muscle strength and tension. Foot orthoses have been found to reduce pelvic misalignment in patients with moderate to severe misalignment [9].

Another class of orthoses are exoskeletons, mechanical devices that were originally designed to enhance the performance of able-bodied individuals [10]. Recently, however, exoskeletons have been developed to restore mobility to individuals who suffer from lower-limb paralysis [10]. New exoskeleton designs, known as hybrid neuroprostheses, combine the stability and support provided by a rigid exoskeleton with functional neuromuscular stimulation, in which healthy muscles that cannot be controlled voluntarily are excited by an external electrical stimulator to move the limbs. These exoskeletons also ensure the limb motion remains within safe physiological limits [11]. Currently, there are only two exoskeletons approved by the Food and Drug Administration (FDA) for the purpose of restoring mobility: ReWalk, which initiates walking motion by detecting upper body tilt, and Ekso Bionics's exoskeleton [12].

Sports

Understanding muscle properties such as the relationship between muscle fiber length and force production, and applying this knowledge to study the biomechanics of movements that are unique to a certain sport, enables the development of training techniques that can enhance athletic performance. For example, new swimming world records in the 1970s are highly correlated with research conducted in the previous decade that highlighted the importance of hand posture for swimmers [13]. Another aspect of sports that relies on motion analysis is study of the terrain on which activities are performed. For example, the stiffness of an indoor running track built by Harvard University in the 1970s was tuned to increase the performance of the athletes while reducing injury risk [14]. Human movement analysis is also used to study individuals during team sports, such as tracking specific player movements during a game [15].

Injury treatment and prevention

Movement analysis can be used to investigate how to prevent injuries in a workplace environment, such as in industrial jobs and for healthcare workers. For example, biomechanical models have been used to determine what part of the population is able to safely apply the necessary forces to perform certain tasks. This understanding can prevent a mismatch between the physical capability of a worker and the physical ability demanded by the task. Garg and Kapellusch [16] found that there is a relationship between the rate of back injuries in a job and the ratio of the greatest load to be lifted and a laborer's strength: the greater this ratio, the higher the rate of back injuries. Other studies have shown that shoulder disorders and shoulder/neck pain were associated with jobs that involve abducting the shoulder more than 90° for prolonged periods of time [16].

Biomechanical knowledge can also be applied to rehabilitation, both orthopedic and neurological. Movement analysis in a gait study can be used to obtain the kinematic data required to identify atypical joint motions. For example, the kinematics of patients with multiple sclerosis are measured to assist in surgical planning [17]. Furthermore, joint moments and powers can be computed by combining the kinematic variables with the measured external forces. Movement analysis has revealed that high plantar pressure is linked to foot ulcers in patients with diabetes and peripheral neuropathy by contributing to faster skin breakdown, which motivated the development of therapeutic shoes that reduce this pressure [18].

1.3 Mechanics

Kinematics is the branch of mechanics concerned with the motion of objects without regard to the forces responsible for or produced by this motion. The motion of each body segment in a musculoskeletal model is described by its position and orientation over time. One may describe the kinematics of a body with respect to a static global coordinate system or using body-fixed reference frames to describe relative motion [19]. Both are useful in biomechanics studies.

Inverse kinematics

In the context of human movement analysis, inverse kinematics is the process of computing skeletal joint angles from indirect measurements of the body's motion, such as the trajectories of skin-mounted markers. Specifically, the markers placed on each body segment during a motion capture experiment are used to calculate each body segment's local reference frame. The reference frames fixed to adjacent body segments can then be used to calculate the relative angles between them; derivatives of these angles provide estimates of joint angular velocities and angular accelerations.

In a typical motion capture experiment, each body segment is tracked using a set of "anatomical markers," which are markers placed on anatomical landmarks that have relatively low soft-tissue motion. The trajectories of these markers are then used to calculate anatomical reference frames (see Figure 1.2), which are assumed to represent the motion of the underlying bones. Because anatomical markers may be difficult to track (e.g., if they are occluded from a camera's view during a motion), then another set of "tracking markers" may be used to calculate tracking reference frames. The relationship between a body segment's tracking and anatomical reference frames is assumed to be constant and is calculated using a "static calibration trial," or a single frame of motion capture data in which the subject is standing in a neutral pose. The transformation matrix that describes the relationship (location and orientation) between the tracking and anatomical reference frames on each body segment is assumed to be constant, based on the assumption that no appreciable bone deformation or soft-tissue motion occurs during movement. Although this approach is commonly used, a model's body segments can move beyond physiological limits when using this method, and the body segments can change length since there are no constraints imposed between adjacent segments [20]. This strategy is sometimes referred to as "unconstrained inverse kinematics" because the relationships between adjacent body segments is allowed to vary arbitrarily [20].

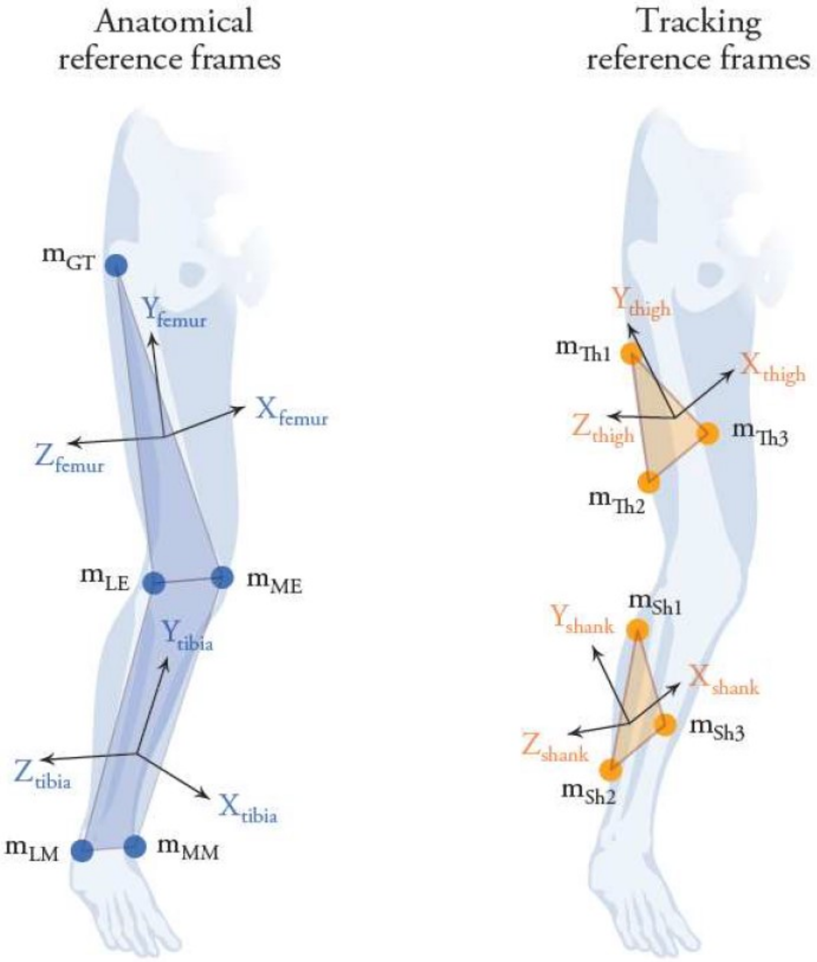

Figure 1.2: Example of anatomical and tracking reference frames on the lower limb. m: marker, GT: greater trochanter, ME/LE: medial/lateral femoral epicondyle, MM/LM: medial/lateral malleolus, Th: thigh, Sh: shank. Image © 2020 David Delp [20].

The "constrained inverse kinematics" approach uses a musculoskeletal model to compute the joint angles of the skeleton while ensuring that the known (or assumed) relationships between adjacent body segments are preserved. The musculoskeletal model is first scaled to match the size and proportions of the human subject. The differences between the positions of the experimental markers and the corresponding markers attached to the model are then reduced through an optimization process. The resulting joint trajectories are typically more accurate than those obtained using the unconstrained inverse kinematics technique. However, the constrained inverse kinematics method relies on a properly scaled model and the markers must be placed on the model in the same anatomical locations as those that were affixed to the subject's skin (i.e., the markers must be correctly "registered") [20].

Inverse dynamics

Once inverse kinematics calculations have been completed and joint angles are known, one can perform an inverse dynamic analysis, which involves computing the forces that were responsible for generating the observed motion. Inverse dynamics can be performed with or without measurements of the ground reaction forces; however, ground reaction force measurements typically increase the accuracy of the results. An inverse dynamic analysis uses Newton's laws of motion to compute net joint moments and net joint loads during a movement, which are necessary to understand and diagnose many movement disorders [20].

Forward kinematics and dynamics

In contrast to inverse kinematics, *forward kinematics* describes the process of computing body-fixed marker locations given the motion of the underlying bones. In robotics, forward kinematics often refers to the calculation of the position and orientation of an end-effector given the joint angles of the robot. In a *forward dynamic* analysis, forces are provided and Newton's laws are used to calculate the resulting motion of the system [20].

1.4 Contributions

The error caused by STA is a problem that is present in all data obtained from experiments that use motion capture systems and skin markers. Usually, each skin marker is assumed to remain at a fixed position relative to the underlying bone throughout the movement studied. It is difficult to account for STA that is present in experimental data during a later analysis phase, which reduces the accuracy of joint calculations and therefore diagnostic capability. To improve the accuracy of inverse kinematics calculations, a model is proposed that includes markers constrained to move on the surfaces of ellipsoids and that are attached to each other via springs and dampers. In this way, the model markers approximate the locations of experimental markers, including the effect of skin stretch. The proposed approach is demonstrated using a model of the upper limb, where improving the accuracy of kinematic calculations could increase its utility in understanding and diagnosing shoulder injuries.

1.5 Thesis organization

The remainder of this thesis is organized as follows. Chapter 2 contains a literature review that describes the anatomy of the shoulder, the common experimental and computational techniques that are used to analyze human movement, and soft-tissue artifacts. In Chapter 3, the proposed method for modelling and simulating skin stretch in OpenSim is presented. The results of this study are presented and discussed in Chapter 4, and conclusions are provided in Chapter 5.

2. Literature Review

In this chapter, some background anatomical information is presented, with a focus on the shoulder. Typical experimental approaches used in human movement analysis are discussed, including a description of their advantages and disadvantages. Popular computational tools are also briefly outlined. The last section of this chapter describes the problem of soft-tissue artifacts in motion capture, discusses the compensation techniques that are currently used, and presents the research question that is addressed in this thesis.

2.1 The shoulder

Anatomy

The musculoskeletal system consists of bones that are connected together by different types of joints to form the basic shape of the body and to provide support and protection for the internal organs. Skeletal muscles move the body by contracting, thereby pulling on the tendons that connect the muscles to the bones. Ligaments are fibrous connective tissues that connect bone to bone and provide stability to joints. Cartilage allows sliding between bones in a joint and acts as a shock absorber. In synovial joints, which are the most common, a viscous fluid called the synovial fluid provides lubrication. These tissues work together to allow us to move with efficiency and versatility [21,22].

The shoulder complex consists of three bones: the humerus of the upper arm, the clavicle or "collarbone", and the scapula or "shoulder blade" (Figure 2.1). These bones are interconnected by four joints: the glenohumeral joint between the glenoid cavity of the scapula and the humerus, the acromioclavicular joint between the acromion (on the scapula) and the clavicle, the sternoclavicular joint between the sternum (breastbone) and the clavicle, and the scapulothoracic joint (generally not considered a "true" joint) which describes the relationship between the motion of the scapula relative to the rib cage [23].

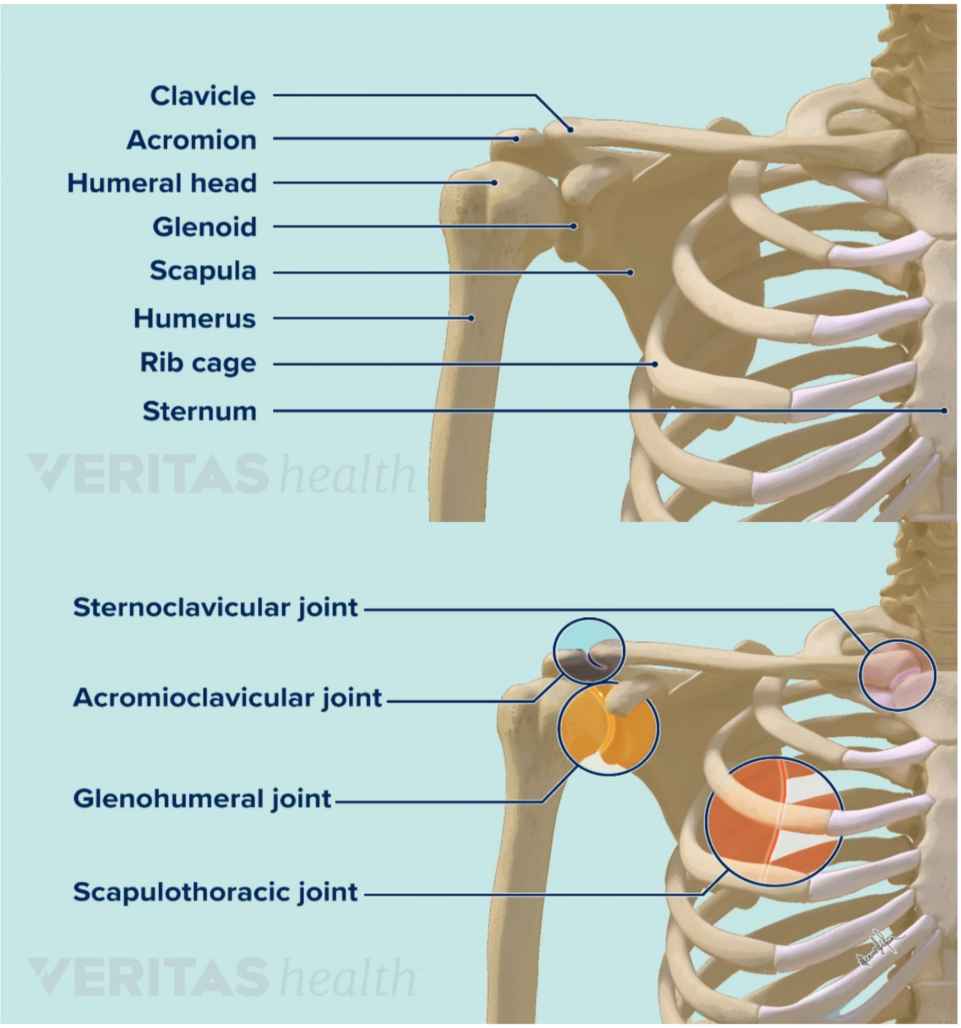

Figure 2.1: The bones and joints of the human shoulder. Reproduced from Novak et al. [24]. Reprinted with permission from VERITAS health.

The movement of the shoulder is stabilized by both passive and active mechanisms. Some of the passive mechanisms include the shape and structure of the glenohumeral joint, which contains cartilage and the glenoid labrum. These structures cover the edges of the joint and provide stability to the humeral head within the glenoid. Other passive stabilizers include the fibrous ligaments (Figure 2.2) that mainly prevent abnormal shoulder translations in different directions. For example, the coracohumeral and superior glenohumeral ligaments help to prevent abnormal inferior and posterior translations of the humeral head during shoulder motion. Dynamic stabilization mechanisms include the rotator cuff muscles, which steer the rotations of the shoulder by pulling on the humeral head within the glenohumeral joint. These muscles also provide stability due to their proximity to the humeral head (the pivot). Specifically, they pull the humeral head into the glenoid when they contract, preventing the humeral head from moving out of the glenoid (i.e., shoulder dislocation). The larger, more superficial muscles such as the deltoid act in force couples at the glenohumeral joint. The passive and dynamic mechanisms present in the shoulder work together to enable stable and versatile shoulder movements [23].

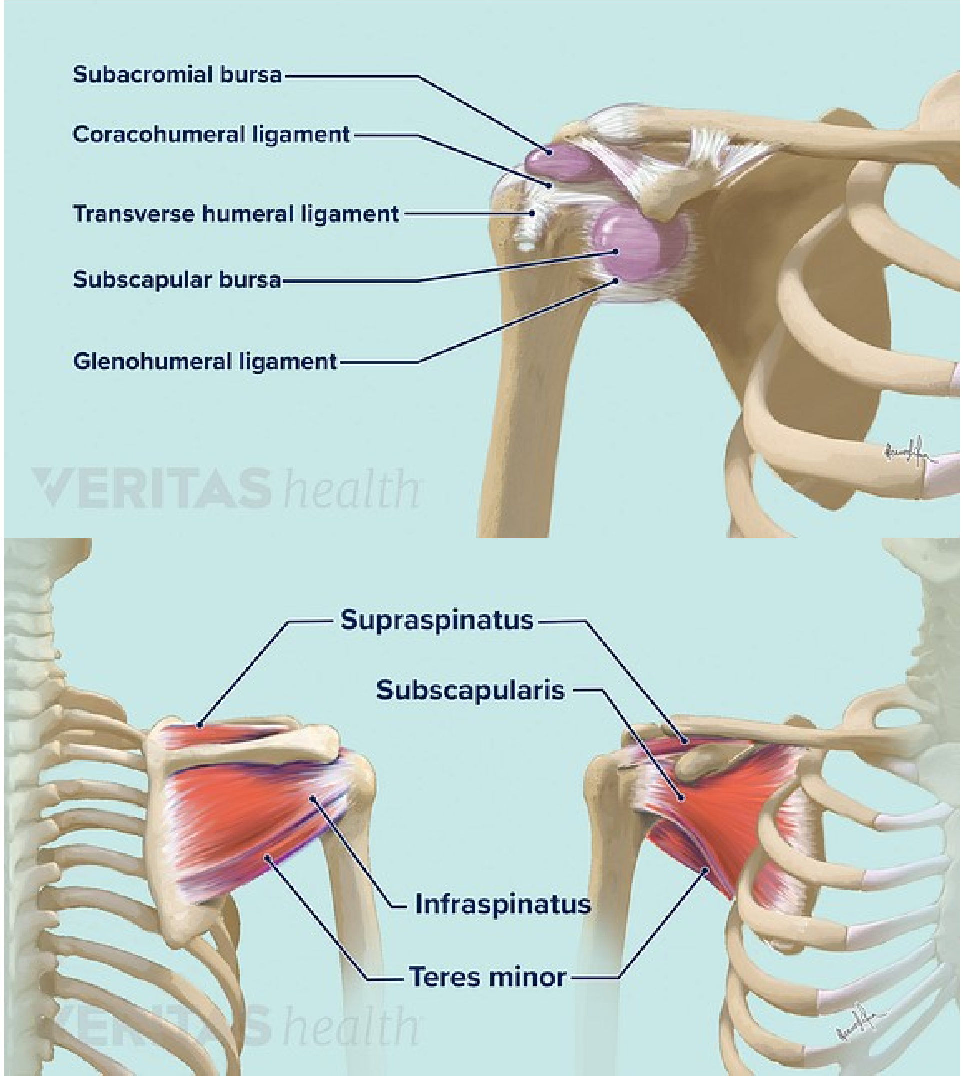

Figure 2.2: The ligaments and bursae (top) and muscles (bottom) of the human shoulder. Reproduced from Novak et al. [24]. Reprinted with permission from VERITAS health.

Common injuries and treatments

In Canada, approximately 544,000 injuries to the shoulder, elbows and arms were reported in a 12-month period between 2009 and 2010, accounting for approximately 11% of injuries in individuals 12–19 years old, 13% in those aged 20–64, and 18% in individuals over age 64 [25].

Rotator cuff tears comprise a group of injuries in which the tendons attaching the rotator cuff muscles to the humeral head are torn. These injuries occur when the tendon is unable to support the amount of force being applied. Shoulder instability is another common condition, often occurring after overextending the shoulder or exposing it to high loads. These conditions can result in the stretching or tearing of the ligaments that hold the joint together, potentially leading to a shoulder dislocation [26]. Relatively minor rotator cuff tears and shoulder instability are usually treated with a combination of physiotherapy, anti-inflammatories and painkillers if the muscle group is largely intact. However, in the case of severe rotator cuff tears, the tendon might not return to its original state and performance without surgical intervention. Furthermore, a history of shoulder instability increases the risk of re-dislocation by up to 90% if it was treated without surgery as opposed to only 25% when treated surgically [27].

2.2 Experimental measurement techniques

Motion capture

Optical motion capture is the most commonly used movement analysis technique because it is non-invasive and fast relative to other techniques. Motion capture involves placing spherical markers on a subject's skin and using cameras to track the motion of these markers as the subject moves. The markers are typically passive, simply reflecting light back to the camera ("retroreflective"). Motion capture systems typically operate in the infrared spectrum so that the markers can be illuminated with stroboscopic light (to avoid motion blur artifacts) without being disruptive to the human subject and researchers. Image processing software can be used to identify each passive marker in each frame of video. Some systems use active markers instead, which generate flashing light in a specific pattern that allows the system to uniquely identify each marker based on the timing of its flashing. The location of each marker in each camera's image is then combined with information collected during system calibration (e.g., the position and orientation of each camera in the lab) to compute the 3D location of each marker in space. The 3D locations of the markers are then used to calculate the position and orientation of each body segment relative to a global reference frame. Finally, the body segment positions and orientations are used to estimate the angles of the joints between them using inverse kinematics (discussed in Chapter 3) [28].

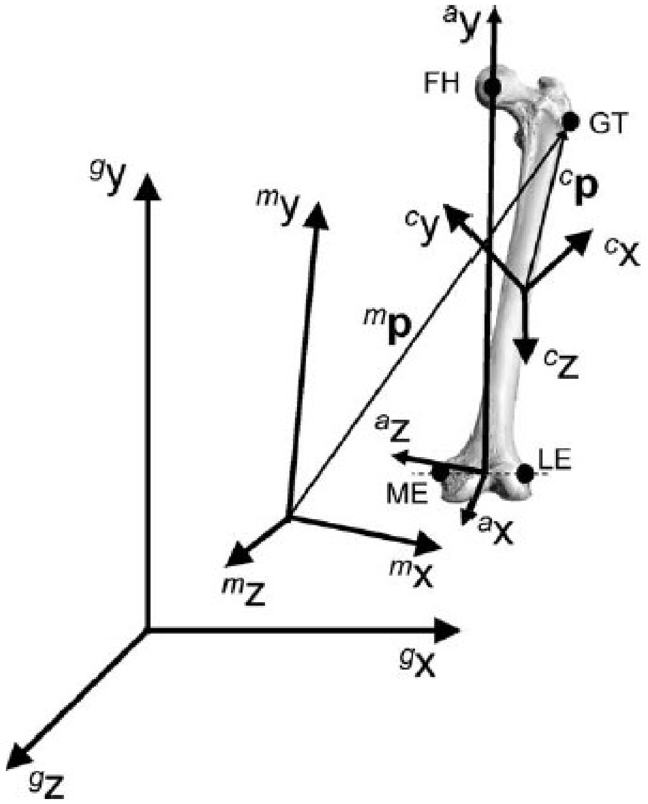

Figure 2.3: Reference frames that are used in inverse kinematics calculations. g, global reference frame; m, convenient intermediate reference frame; a, anatomical frame; c, body-fixed reference frame; GT, greater trochanter; FH, femoral head; ME, medial epicondyle; LE, lateral epicondyle. Reproduced from Cappozzo et al. [29]. Reprinted with permission from Elsevier.

Despite its popularity, optical motion capture is not without its drawbacks. A common source of measurement error occurs when a marker moves out of the view of some of the cameras, which leads to errors in the calculation of the marker's 3D location. Smoothing or interpolation can be used to reduce the effects of this type of error. Errors in calculating a marker location can also occur even when the subject is standing still due to errors in the reconstruction of the 3D marker position by the motion capture system. These errors are typically small if the system has been correctly calibrated. Finally, the markers that are placed on the skin are assumed to be fixed relative to the underlying bones, which is incorrect due to the motion of soft tissue (e.g., skin stretching, muscles bulging and the wobbling of fat). Soft-tissue motion leads to relative movement between the marker and the bone. Reducing this type of error, known as the soft-tissue artifact (STA) [28], is the focus of this thesis.

Inertial measurement units

Inertial measurement units (IMUs) are compact wireless devices containing gyroscopes and accelerometers that enable the measurement of the angular velocities and linear accelerations of each body segment. Because the system does not rely on cameras to track the subject's movement, IMUs can be used to measure kinematic data in real-world settings rather than a synthetic laboratory setting. Additionally, IMU systems have been shown to produce similar kinematic results to high-quality marker-based systems, and are relatively inexpensive. IMU systems can also include a movement classification system that provides the wearer with feedback, such as information about whether they are performing an exercise correctly for rehabilitation purposes.

Classification systems can be personalized, analyzing data from a single individual, or generic, using data from multiple people to make more general observations.

IMU systems are continuing to improve in accuracy and grow in popularity; however, optical motion capture systems are still more accurate than IMU-based systems in many situations. Personalized movement classification systems require large amounts of data and must be trained specifically for each patient, which is time consuming and prevents clinical adoption of IMUs. It is also common for IMUs to slide relative to the skin, which makes collection of high-quality data difficult. IMU systems are still under development and being validated, and they are improving rapidly [30].

Bone pins

Bone locations can be measured directly by implanting into the bones a set of pins that protrude from the skin and attaching markers onto these pins. The markers are then tracked by a motion capture system to obtain highly accurate measurements of bone locations. The appropriate size of the pin depends on many factors, including the amount of soft tissue present and the size of the bone into which it is being inserted. Because the pins are directly attached to the bones, the markers are not affected by the large measurement errors that typically occur due to the movement of the skin relative to the bone. Due to the high accuracy of this technique, “bone pin data” are often used to validate other measurement strategies.

The use of bone pins for studying movement has several downsides and is not error-free. Bone pins can bend and become loose due to the movement of the surrounding soft tissue, thereby also affecting the movement of the markers. Smaller pins are more susceptible to being affected by the surrounding tissue and larger pins risk causing injury to the subject. Furthermore, studies that use bone pins usually have a very low sample size due to the invasive nature of this technique, and the subjects might alter their movement due to the presence of the pins. Although bone pins have these issues, they are still one of the best tools to accurately calculate joint angles during movement [31].

Fluoroscopy

X-ray fluoroscopy is a technique in which a series of X-ray images is captured to track the movement of bones and skin markers without restricting the movement of the skin via pins or other external devices [32]. This technique usually entails the use of either 3D computer-aided design (CAD) models of implants or CT/MRI scans of bone morphology to be able to translate the 2D images into 3D movements. However, the field of view is very small which limits the body segments that can be captured at high resolution; thus, this technique is also limited in the types of movements that it can be used to study. Recent studies have proposed a mobile fluoroscope to enable measurements of movements that would not be possible using a static fluoroscope due to the limited field of view [33].

Biplanar fluoroscopy involves taking X-ray pictures simultaneously in two planes. This technique is widely used in surgeries that require a series of X-ray images at several limb positions [34]. A study by Westberry et al. showed that, once surgeons learned how to use biplanar fluoroscopy, they did not return to single-plane fluoroscopy because the biplanar machine increases surgical accuracy and does not require a long set-up time [35]. In biplanar fluoroscopy, an X-ray picture is taken in each plane by a C-arm device, which comprises a C-shaped arm that emits X-rays from one end and captures them on the other end (see Figure 2.4) [36]. However, in biomechanical studies, biplanar fluoroscopy imposes substantial restrictions on the movement of the subject and thus is seldom used for this purpose [37].


[redacted]

Figure 2.4: C-Arm machines. Reproduced from Tsai et al. [36]. Reprinted with permission from Elsevier.

Force plates

Force plates are devices that are often used in motion capture experiments to quantify the forces and torques that are acting between the ground and the subject's feet. Force plates provide the magnitude and direction of these forces and torques, often referred to collectively as "ground reaction forces," through measurements from load cells located at the corners of the plate. Knowledge of the ground reaction forces allows us to apply Newton's laws to compute the net joint moments acting at the skeletal joints. Force plates are very accurate if correctly calibrated, but experience chemical, thermal and electrical noise as well as hysteresis which can lead to erroneous measurements [38].

2.3 Computational methods

ADAMS

ADAMS, Automatic Dynamic Analysis of Mechanical Systems (MSC Software), is a widely used software package for modelling and simulating multibody systems comprising rigid and/or flexible bodies [39]. ADAMS has been used in biomechanics studies to compute the forces in muscles, ligaments, cartilage, and other tissue during movement [40]. ADAMS also has a plugin called LifeMOD, which is specifically designed for use in biomechanical studies [41]. LifeMOD allows one to build custom human models by entering parameters such as the height, weight and age of the subject. These parameters are then used to automatically generate an approximate human model based on anthropometric databases. It also allows importing of formatted MRI and CT scan data and geometry from computer-aided design systems. Furthermore, motion capture marker data can be imported to move the model [42].

OpenSim

OpenSim is an open-source software package for modelling and simulating human and animal movement [43]. It allows one to use prebuilt models or to create new models of the neural, muscular, and skeletal systems for generating simulations from motion capture data. OpenSim is often used to calculate quantities that are difficult to measure directly, such as the force generated by an individual muscle during a movement [44]. OpenSim is typically used in one of two ways: to reproduce an observed motion that was recorded in the lab or to predict movement based on models of neural controllers. An example of the latter is the study performed by Dorn et al. to predict the changes that would occur (e.g., in muscle activity) when walking on an inclined surface [45]. The program also allows users to extend the software by creating plugins using C++, which facilitates sharing resources with other researchers [46]. Current uses of OpenSim include studying the structure of the limbs and their function [47,48], in the development of exoskeletons and implantable devices [49–51], and in researching the importance of reflexes in movement [52]. In this thesis, OpenSim is used because it is open source and modular, which allows changes to be implemented more easily compared to other software. Furthermore, many projects and resources have been built with OpenSim that have been tested and validated are readily available for use.

AnyBody

AnyBody is a modelling and simulation software package with a complex full-body musculoskeletal model containing 458 muscles [53]. The model parameters, such as height and body proportions, are easily adjustable by the user. Like OpenSim, the program allows one to create custom models, such as musculoskeletal models of different animals. However, the program must be purchased for use and it uses its own Anyscript scripting language for modelling which can be a barrier for new users [53]. Additionally, OpenSim is open source which allows users to inspect the underlying algorithms, extend them and share them with other users; AnyBody is closed source so its algorithms are difficult to study and extend.

2.4 Soft-tissue artifacts

Biology

The three layers that make up the skin are the epidermis and dermis (together known as the cutis), and the hypodermis (Figure 2.5). The protein fibers collagen, elastin and reticulin are present within the dermis layer. Collagen makes up 18–30% of the dermis layer volume and only starts to straighten when the skin is strained by approximately 30%. Elastin makes up approximately 1% of the dermis volume and is responsible for skin mechanics at low strains and skin recoil (return to neutral state after being stretched). The third and deepest layer, the hypodermis, contains adipose (fat) cells and accounts for approximately 10% of the entire body mass. The thickness of the hypodermis layer differs between body segments and individuals.

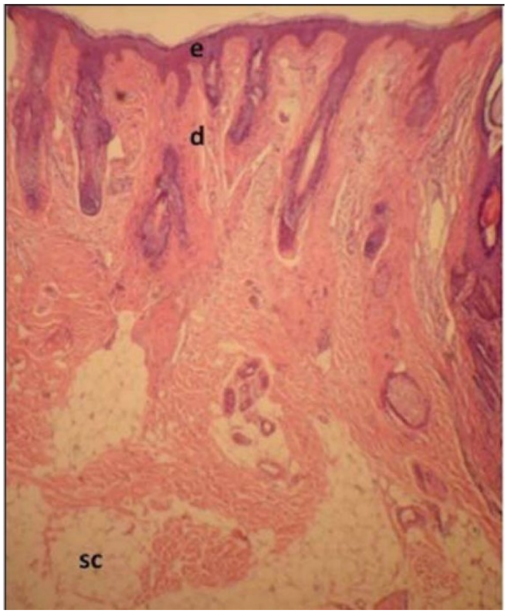

Figure 2.5: The layers of human skin. The three major layers of skin. e: epidermis, d: dermis, sc: hypodermis (subcutaneous tissue). Reproduced from Barcaui et al. [54]; licensed under Creative Commons Attribution License.

The skin displays a nonlinear stress–strain relationship that can be divided into three stages (Figure 2.6). In stage I, the skin undergoes large deformations (strain) under relatively small amounts of force (stress). In this stage, only elastin is producing force; the collagen fibers are wound and do not produce any force. Next is stage II, during which the collagen fibers start unwinding and resist stretch, leading to a rapidly increasing overall skin stiffness (i.e., strain increases less and less in response to the same incremental increase in force). Stage III is characterized by completely unwound collagen fibers and a linear stress–strain relationship [56]. The skin's stress–strain curve can also change over time upon repeated cyclic loading [55].

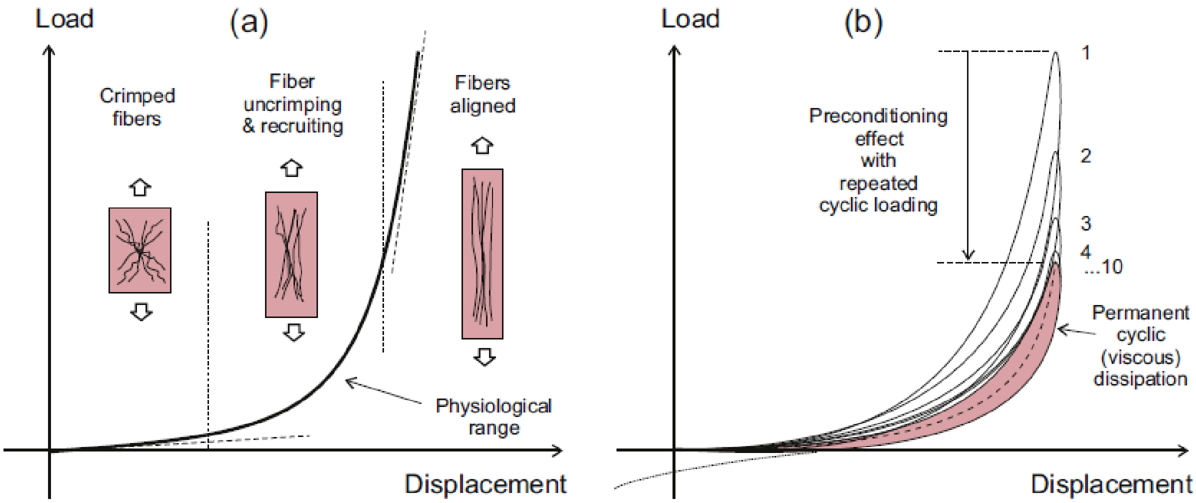

Figure 2.6: State of collagen fibers in each of the three skin stretch regions and preconditioning of skin. a. Stress–strain curve of the skin. The stiffness of collagen fibers is constant in the first stage, then increases with increasing strain in the second stage (skin is in this stage most of the time), and becomes linear again in the third stage. b. Effect of cyclic loading on skin. Adapted from Benitez et al. [55]. Reprinted with permission from Elsevier.

Anisotropy

Skin is naturally under tension in vivo and is anisotropic, meaning that the amount of strain the skin undergoes will differ depending on the direction in which a force is applied. This can be observed when a small slice is made in the skin, causing the skin to retract on either side. Different amounts of skin retraction will be observed following an incision depending on the location and angle of the slice. Langer lines (Figure 2.7A), identified by A. K. Langer, are lines on the skin which run parallel to the majority of collagen fibers. The collagen fibers perpendicular to the lines are less stretched in the natural state than the collagen fibers parallel to the Langer lines.

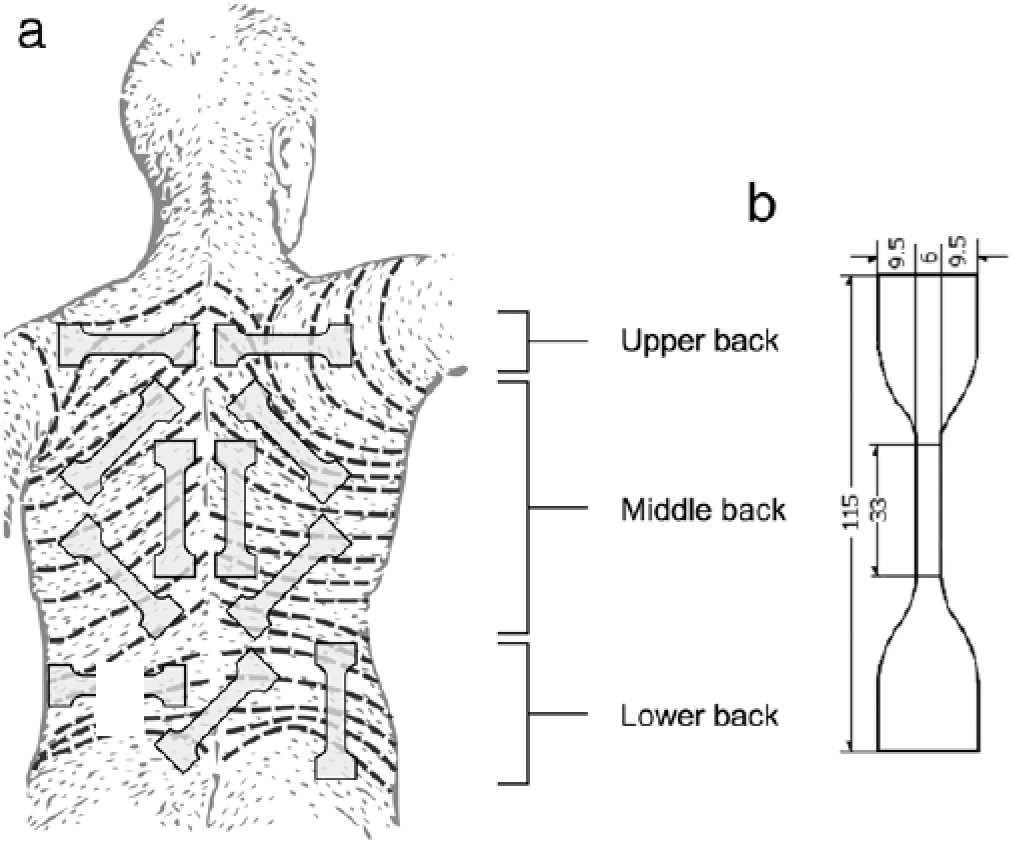

Figure 2.7: Langer lines. a. Dashed lines show Langer lines on the human back, and excisions made to cadavers. b. Dimensions of excisions (in mm). Reproduced from Annaidh et al. [57]. Reprinted with permission from Elsevier.

As can be seen in Figure 2.8 below, more stress is needed to produce the same amount of strain when applied parallel to the Langer lines [56]. This feature of skin is important to consider in surgical procedures because skin scars become unsightly and more elongated when closed under tension [58]. Although Langer lines have proven to be useful in surgeries and forensic medicine, nowadays surgical incisions follow Langer lines only in certain body areas; other lines such as relaxed skin tension lines might also be used [59].

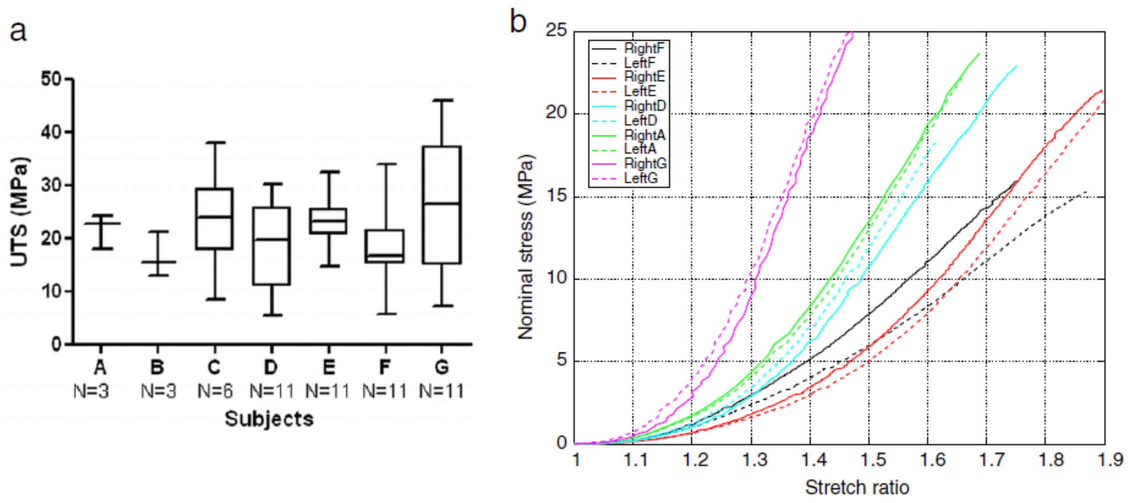

Figure 2.8: Mechanical properties of excised skin. a. Ultimate tensile strength of different skin samples from body segments of same individual. b. Stress–strain curves of excised human skin from five cadavers (labelled A, D, E, F and G in the legend). “Left” and “right” labels indicate the excisions from the left and right sides of the upper back, as shown in Figure 2.7a. Reproduced from Annaidh et al. [57]. Reprinted with permission from Elsevier.

Measurement techniques

Suitable strategies for measuring the properties of human skin depend on whether the study involves using excised human skin or live subjects. Excised human skin can be studied through tensile stress testing in different directions to provide the stress–strain curves of the skin while considering Langer lines. Furthermore, the different layers of skin can be separated to suit the specific purpose of the study, as was done by Annaidh et al. [57]. In-vivo testing methods include indentation tests in which force is applied to the skin, torsion tests in which the skin is rotated, and suction tests in which the skin is lifted in a hole [60].

Modelling of skin

Several finite element models have been developed to study the behaviour of human skin. A precise model of human skin must consider that the skin is viscoelastic and anisotropic [61]. The skin's several layers have different properties; bones and muscles can also affect the properties of the skin. Furthermore, the model properties will depend on the body segment being modelled, as well as the body mass index (BMI), age and gender of the subject [61].

Effects on motion capture data

In motion capture experiments, the skin-mounted markers move relative to the underlying bones due to the stretching and sliding of skin, bulging of muscle, and other soft-tissue motion, collectively known as soft-tissue artifacts (STA). STA is a source of error in the ensuing kinematic analysis, affecting the calculation of skeletal joint angles. Invasive methods such as bone pins can be used to measure the effect of STA; however, the presence of the bone pins can cause the tissue to behave differently. X-ray fluoroscopy can be used to measure the effect of STA in a kinematic analysis without altering the movement of the tissue as it does not require implants; however, fluoroscopy exposes the subject to ionizing radiation and thus is not appropriate for all studies. The amount of STA error differs between subjects, the activity being carried out, the marker location, and in each of the anatomical directions. Consequently, different amounts of STA have been reported in different studies [62].

Specifically for the shoulder, a study by Bourne et al. demonstrated that digitizing anatomical landmarks provides more accurate results for scapular kinematics [63]. Digitization involved the use of an optoelectronic probe to palpate areas on the spine, humerus and scapula to deal with the sliding of the scapula underneath the skin [63]. Results showed that subjects with the highest BMI had the highest errors. Furthermore, they found that digitization did not improve accuracy at full abduction, which is the most important position to study as shoulder problems are usually associated with overhead activity [63].

Compensation techniques

Several post-processing strategies have been used to compensate for STA when it exists in movement data. Filtering techniques are often insufficient to remove STA because the frequency of the soft-tissue motion (noise) is in the same range as the frequency of the movement being tracked (signal). Other strategies include the pliant surface modelling method, which models the soft-tissue motion on the surface of a body segment using computer graphics techniques [64]. Another strategy is the multiple anatomical landmark calibration technique, which involves computing the relationship between anatomical and tracking frames at both extremes of the expected motion and interpolating this relationship over the motion [64]. This strategy may be preferred over the static calibration technique, which relates anatomical and tracking frames using a single frame of motion capture data, because the relationship between skin markers and anatomical landmarks changes with the position of the body [20]. Finally, optimization can be used to minimize the difference between measured marker positions and predicted marker positions in a model containing kinematic constraints (see Section 1.4) [65].

Another technique uses triangular cosserat point elements (TCPEs), which are triangles created by picking different sets of three markers from among all the markers placed on the subject. The result is that a different set of triangles is produced at each time step of the motion. A specific set of markers is chosen at each step that is thought to result in the most accurate bone pose considering STA [66]. In theory, if the best set of markers is chosen at each time step, the errors are reduced. The best possible marker set (TCPE subset) is selected by considering the strain in the TCPE, and the relative translations and rotations between TCPEs [66].

Research question

Given the large number of injuries related to the shoulder and the complexity of its structure, accurate measurement techniques are needed for in-depth analysis of shoulder biomechanics. Invasive measurement techniques excel in obtaining accurate data sets, but fall short in other aspects such as very small sample sizes in bone pin studies. Non-invasive measurement techniques, more specifically motion capture systems, are far more popular and are commonly used in biomechanical research. However, motion capture studies suffer from STA errors that reduce the accuracy of their conclusions. Various techniques have been developed to reduce STA-related errors and have varying effectiveness. Our research question is as follows: Would a model that combines constrained kinematics, physiological limits to joint angles, and in particular skin stretch modelling provide better calculations of marker positions, and would it help increase the accuracy of the obtained kinematic variables from an inverse kinematic solution?

3. Methods

This chapter begins with an outline of how the scaling, inverse kinematics and forward dynamics calculations are performed in OpenSim. Second, the methodology behind the scapulothoracic joint model on which our work is based is summarized. Third, the development of the proposed upper-extremity model is discussed, from the initial test models to the final model, and the strategy that was used to build it. Finally, an explanation of the optimization method used to calculate the model coordinate values taking the motion of the skin into account is provided.

This study uses experimental data obtained by Ludewig et al. [67]. In the study by Ludewig et al., bone pins were used to track shoulder abduction, flexion and rotation motions of twelve subjects. The experimental data do not include skin marker data, so for the present study, synthetic skin marker trajectories were generated by introducing three sets of four makers each into the OpenSim model. The center of each of these sets of four markers is assumed to represent the position of a skin-mounted marker. The markers were assembled in a mesh and were constrained to move on the surface of a nearly flat ellipsoid to represent the skin stretching over the surface of the scapula.

This study focuses on the abduction motion from the experimental data of Ludewig et al. [67]. The motion is divided into time steps. At each time step, a dynamic simulation is run to allow the markers of the mesh (the "synthetic skin") to reach equilibrium; the final position is assumed to represent the skin at that time step during the experiment. Using this technique, synthetic skin marker trajectories were generated using the bone pin data of Ludewig et al. These trajectories are used as the “targets” for an optimization problem. An optimizer is then used to calculate the model’s joint coordinates while considering skin stretch. The objective function of the optimizer is the sum of the distances between three pairs of synthetic skin markers, each pair comprising one marker on the skin in the dynamic simulation and one “target” skin marker position. At each time step, the optimizer evaluates many candidate solutions (sets of model joint coordinates), allows the marker mesh to settle, and then calculates the distances between the three marker pairs. This process is repeated until the objective function value is below a predetermined threshold (or the maximum allowable number of candidate solutions has been evaluated). The methodology is described in more detail below.

3.1 OpenSim

This section provides a description of the computational workflow that is used to generate simulations in OpenSim from motion capture data.

Scale Tool

In OpenSim, body segments are modelled as rigid bodies, as defined by a reference frame, a center of mass, and inertial properties [68]. Generic models must be scaled to match the size of the participant. First, scale factors are determined for each body segment. Scale factors can be entered manually or calculated automatically by comparing the locations of experimental motion capture markers with the locations of the corresponding markers attached to the model (see Figure 3.1). In the latter case, a single frame of motion capture data is typically used, where the subject is standing in a neutral pose. The scale factors are then used to scale each body segment in each dimension (while respecting the constraints imposed by the kinematic joints of the model) to minimize the distance between each pair of experimental and model markers. Finally, the model marker locations are typically adjusted so that they match the locations of the corresponding experimental markers exactly [69].

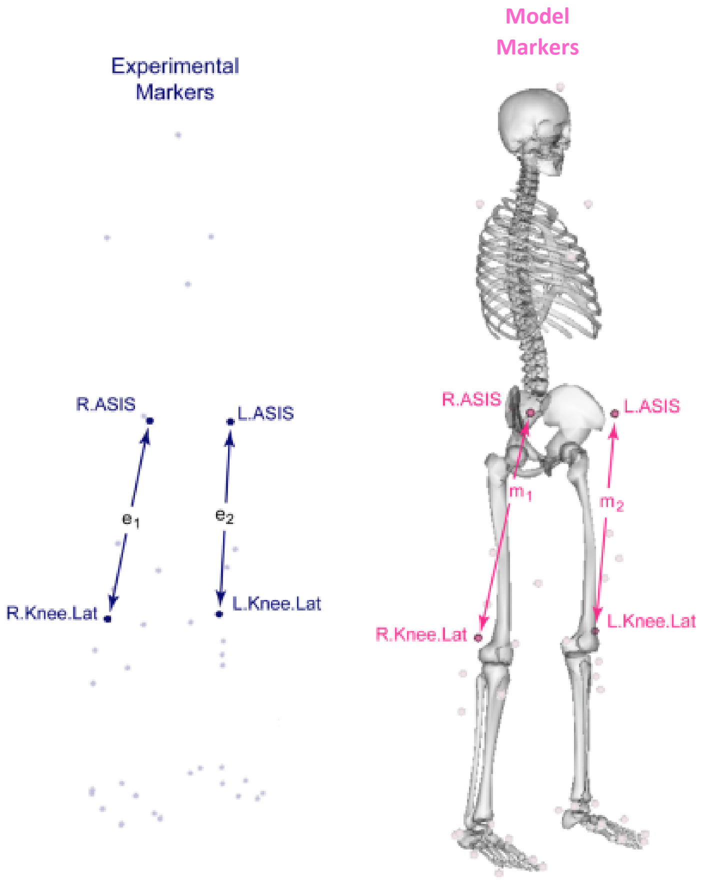

Figure 3.1: Experimental and model marker pairs used to scale a musculoskeletal model. Distances e_1 and e_2 (computed from the experimental data, left) are compared with distances m_1 and m_2 (computed from the model, right) to obtain scale factors. This process is repeated for several pairs of markers and for each body segment in the model. Image copyright © 2009–2021 Stanford University [69] and reproduced with permission under the MIT License.

Inverse kinematics

In an inverse kinematic analysis, OpenSim computes the coordinates (joint angles) of the model such that the location of the model markers in space are as close as possible to those of the experimental markers in each time step of the motion. OpenSim uses a weighted least-squares algorithm, where the user provides weights that determine the relative importance of tracking each marker. The model's coordinates can also be tracked explicitly, if these data are available. Joint angles may be measured directly during an experiment, computed by the motion capture system, or estimated by another algorithm [70].

Forward dynamics

In OpenSim, the user can predict movement by generating a forward dynamic simulation, wherein the ordinary differential equations that describe the dynamic behaviour of the model are integrated forward in time. Forces and/or muscle excitations may be provided and applied to the model during the simulation [71]. The Forward Dynamics Tool is used in the present study to simulate the behaviour of the skin (described in Section 3.4).

3.2 Seth's scapulothoracic joint model

A model of the scapulothoracic joint with constrained kinematics was built by Dr. Ajay Seth at Stanford University with the goal of disallowing non-physiological motions of the scapula that would otherwise occur in a kinematically unconstrained model, such as translation of the scapula normal to the surface of the thorax [72]. The model includes a new type of joint, the "scapulothoracic" joint, which limits the motion of the scapula to the thoracic surface as represented by an ellipsoid. As shown in Figure 3.2, the model permits only physiologically possible motions of the scapula: abduction/adduction, elevation/depression, internal rotation (about the Y-axis), and upward rotation (about the Z-axis). Notably, the model does not permit rotation about the X-axis or translation along the Z-axis (directed into or away from the surface of the thorax) [72].

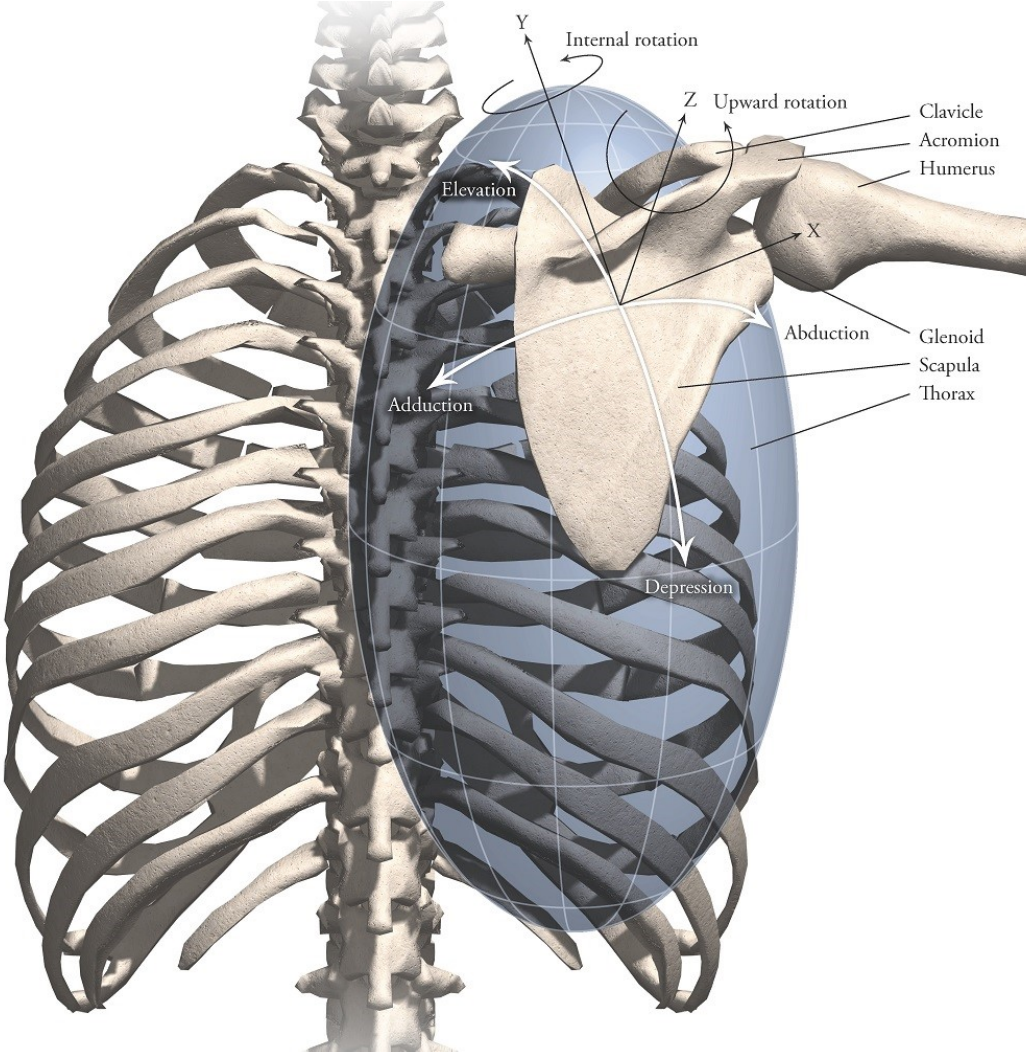

Figure 3.2: Scapular motions in Seth's upper-extremity model. Image © 2020 David Delp [20].

Seth validated his model by adding Gaussian noise, translational and rotational offsets, and "warping" to bone pin marker positions to simulate markers that are placed on the skin [72]. Scapular inverse kinematics results obtained from Seth's model were more robust to measurement noise than results obtained by calculating joint angles from marker locations without the constraints of the scapulothoracic joint. The scapulothoracic joint allowed the model to withstand up to 20 mm of noise in the marker locations while still producing clinically meaningful results, compared to the 8 mm noise limit of a model that does not have these kinematic constraints (Figure 3.3). Furthermore, the model results closely matched the kinematic values obtained using bone pins, which are considered to be the "gold standard" in measuring kinematic variables [72,73]. The error threshold for clinically meaningful results varies between activities [74]. A study by Bourne et al. on six subjects showed that the intra-subject root mean square error variability in upward rotation was between 1.1° and 4.7° [74]. Seth et al. used 4.7° as the threshold for clinically meaningful results [72].

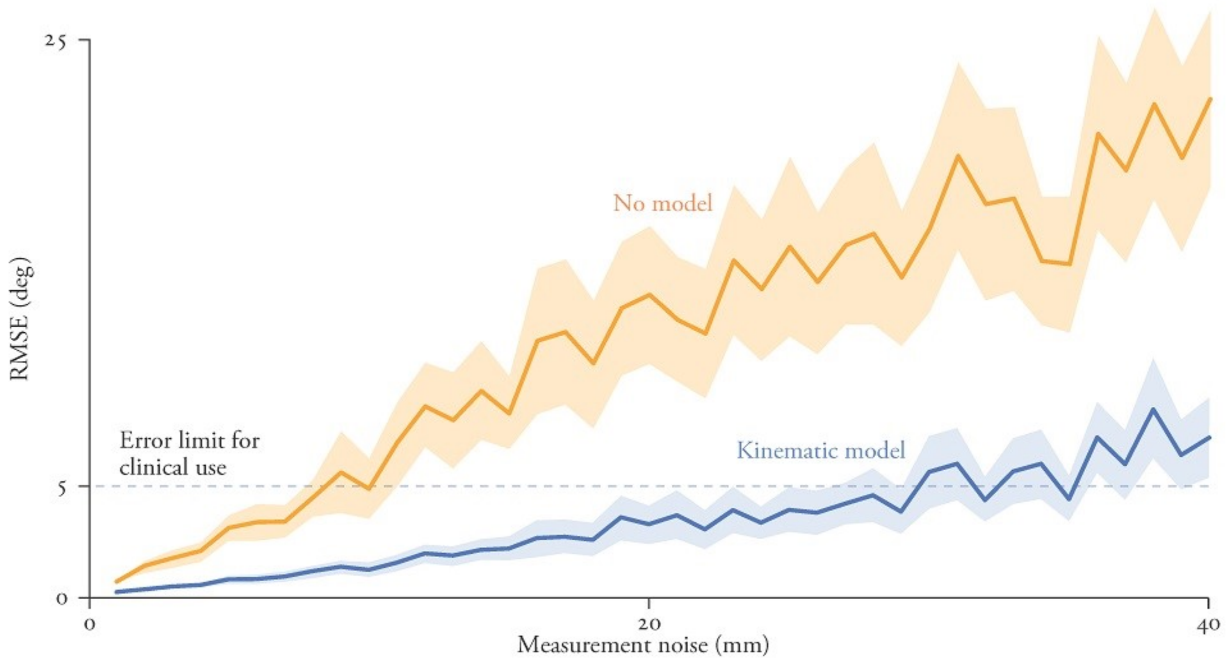

Figure 3.3: Change in root mean square error (RMSE) in joint angles calculated using Seth's upper-extremity model as measurement noise is increased. Orange and blue data indicate the RMSE without and with the kinematic model, respectively (mean, line; standard deviation, shaded). Image © 2020 David Delp [20].

The experimental data used by Seth comes from a study performed by Ludewig et al. involving twelve subjects [67]. Three bone pins were inserted into each subject: one on the acromion of the scapula, one in the middle of the clavicle, and one on the lateral side of the humerus where the deltoid attaches [67]. Markers were attached to each of these pins; another marker was placed on the sternum. Correct insertion of the bone pins was ensured using mini-fluoroscopy [67]. The subjects performed three shoulder motions: abduction, flexion and rotation. The subjects were also asked to perform the entire motion in six seconds, reaching peak abduction, flexion or rotation after three seconds. The abduction motion involved raising the arm along the coronal plane with the thumb pointed up, the flexion motion involved raising the arm along the sagittal plane, and the rotation motion was performed with the arm raised between the coronal and sagittal planes. The joint angles were calculated through inverse kinematics and the results from the twelve subjects were averaged [67]. The paper by Seth et al. refers to "a subject" [72], but details about the subject's BMI, height, weight, etc. were not provided.

3.3 Experimentation

The goal of the proposed model is to simulate skin stretching and moving relative to the underlying bones. The positions of skin-mounted markers depend on these effects and it is hypothesized that more accurate joint angles can be obtained if these effects are considered in the model. Figure 3.4 outlines the processes involved.

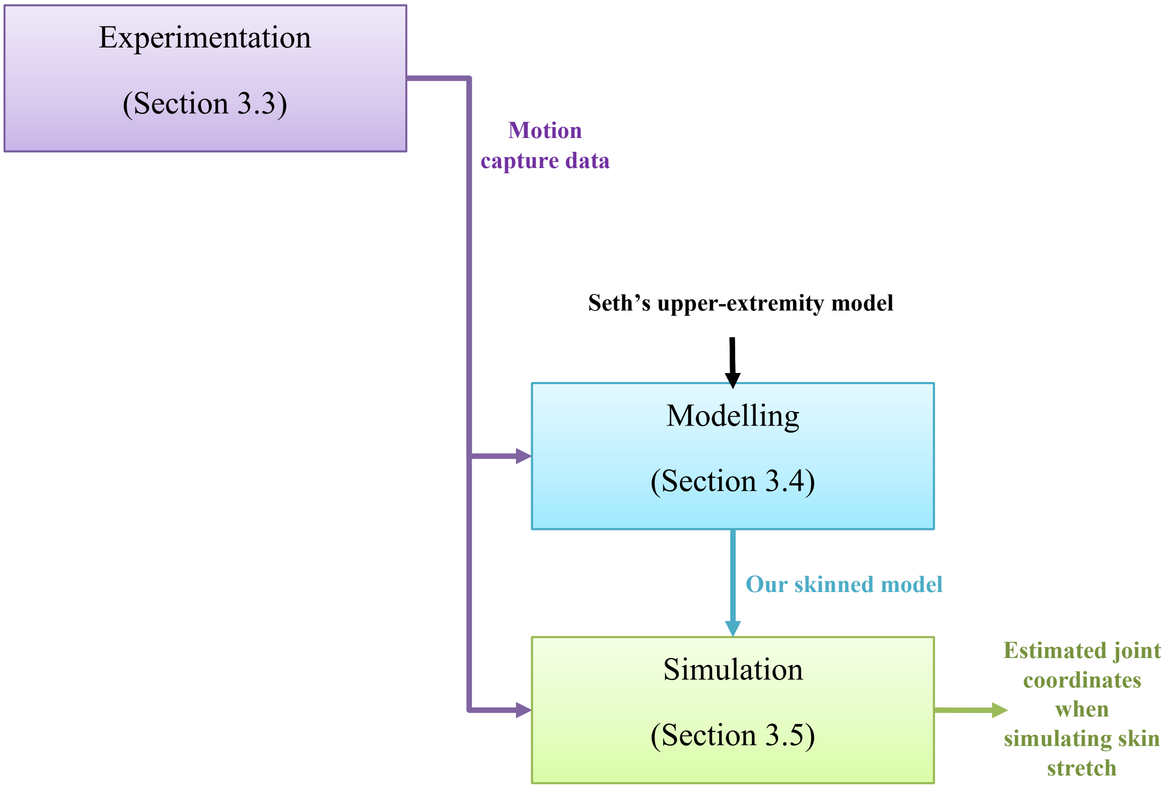

Figure 3.4: Outline of processes to estimate joint coordinates when simulating skin stretch.

To simulate these effects, the experimental bone pin marker data provided by Ludewig et al. [63] is used. Figure 3.5 outlines the processes they used to obtain their experimental data, as described above (in Section 3.2).

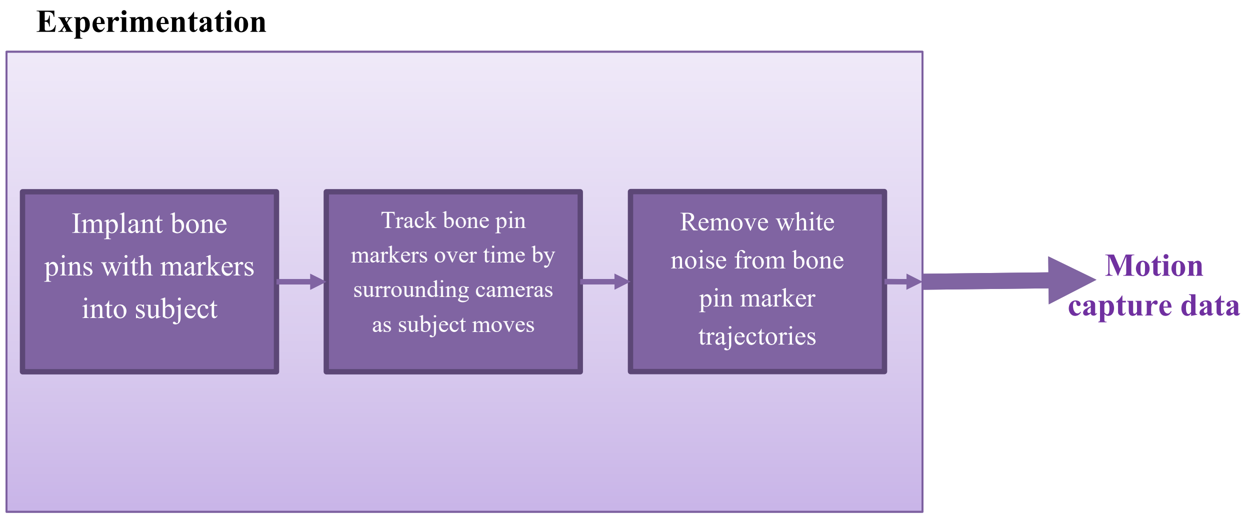

Figure 3.5: Experimental process used by Ludewig et al. [67].

3.4 Modelling

This section provides a description of how the proposed model was built, based on Seth's upper-extremity model; the processes used are shown in Figure 3.6. Briefly, the ellipsoids that represent the body segments were added first. Then, float bodies, anchor bodies and markers were added, where the float bodies move (float) on the surface of the ellipsoids and the anchor bodies remain fixed relative to the ellipsoids. These new bodies were then attached to each other by springs and dampers. Model coordinate values, obtained through inverse kinematics using the bone pin data, were used to move the model to its default position. The float bodies were then moved into the desired configuration on the surface of the ellipsoids. Four sets of four float bodies each were arranged in a rectangular pattern on the surface of the scapula; these boxes are used to estimate the location of skin-mounted markers. These steps are explained in more detail below.

Background

The proposed model is based on Seth's upper-extremity model (see Figure 3.7), which is built around his model of the scapulothoracic joint. The goal of the proposed model was to further reduce the effect of STA on inverse kinematics calculations by explicitly modelling the effect of skin stretch on the locations of skin-mounted markers. To construct the proposed model, Seth's model was augmented with 4 ellipsoids that approximate the shape of the skin surface of the thorax, abdomen, upper arm and scapula (red ellipsoids in Figure 3.8). In this work, the size and shape of each ellipsoid were determined manually to approximate the surface of the body as a proof of concept; MRI or other imaging data could be used to improve accuracy, if such data are available. The thorax and abdomen ellipsoids were "welded" (rigidly attached to) the rigid body comprising the rib cage, sternum, and vertebrae; the upper-arm ellipsoid was welded to the humerus bone; and the scapula ellipsoid was welded to the scapula body.

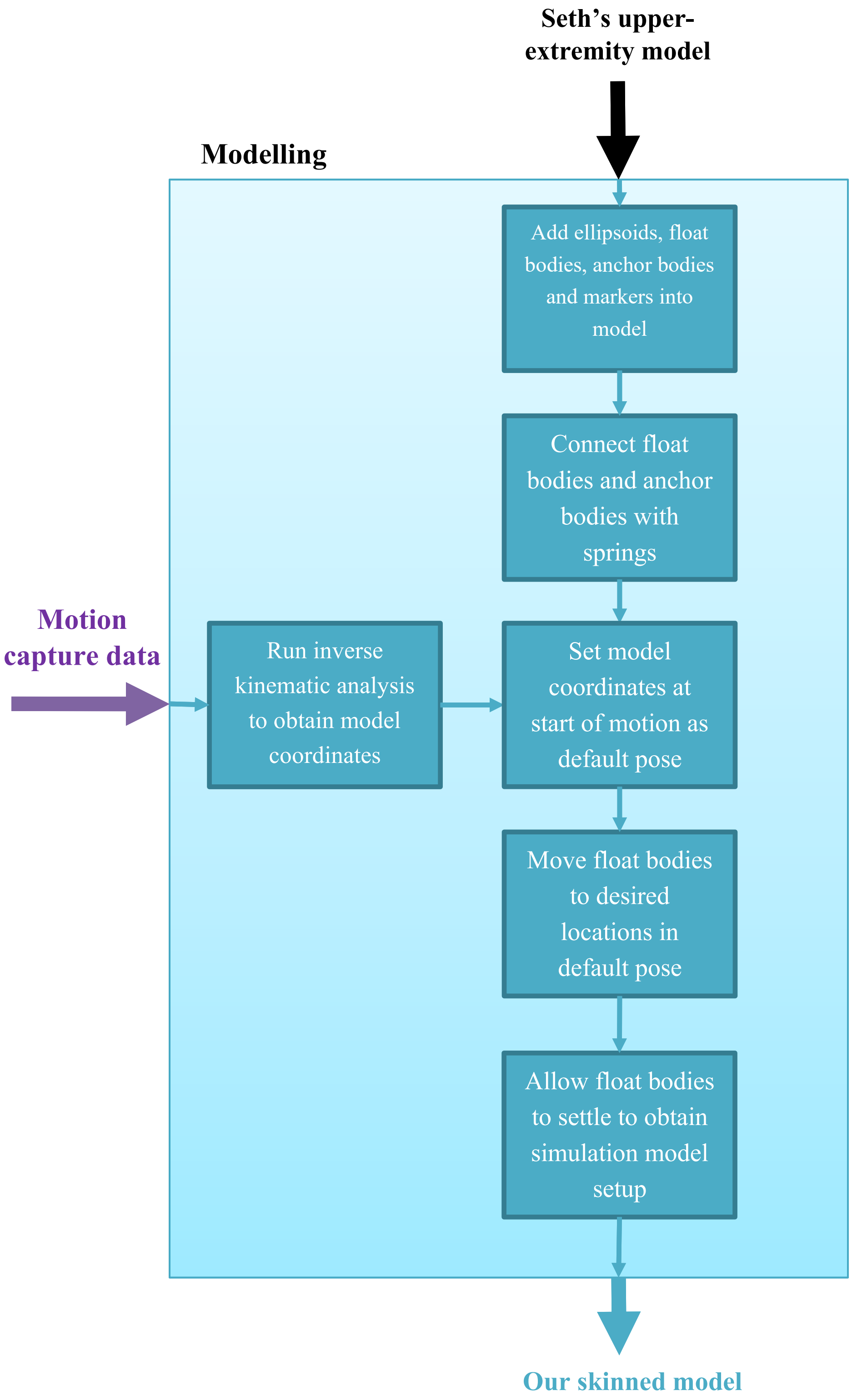

Figure 3.6: Modelling strategy that was used to produce the proposed skinned upper-extremity model.

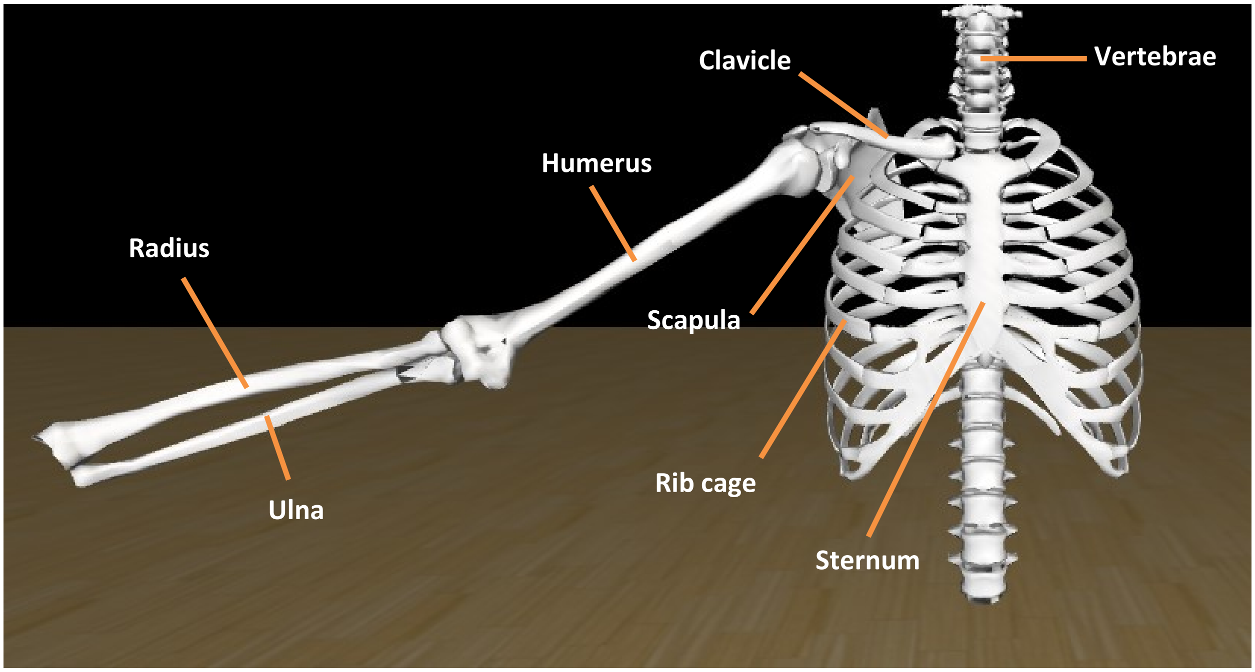

Figure 3.7: Seth's upper-extremity model consisting of a torso and the right arm and shoulder. The vertebrae, rib cage and sternum make up one rigid body called the thorax. Movements involving the scapula, clavicle and humerus (comprising the shoulder complex) are controlled via 9 model coordinates. The radius and ulna can move only by pronation/supination and elbow flexion.

Once the ellipsoids had been defined, a small number of rigid bodies were added to the model. The bodies were constrained to glide on the surface of the ellipsoids. Some of these bodies were placed around the perimeter of the area interest. These bodies, referred to herein as "anchors," are fixed—that is, they do not move relative to the underlying bones. The anchors define points on the skin that are assumed to remain stationary relative to the bones during the movements that were analyzed in this study. (Note that the appropriate placement of anchors may differ for different motions.) Additional bodies, referred to as "float bodies," were placed on the body segment ellipsoids. The float bodies are free to move (float) on the surface of the ellipsoids, representing points on the skin that move relative to the underlying bones. These bodies also have manually selected masses associated with them.

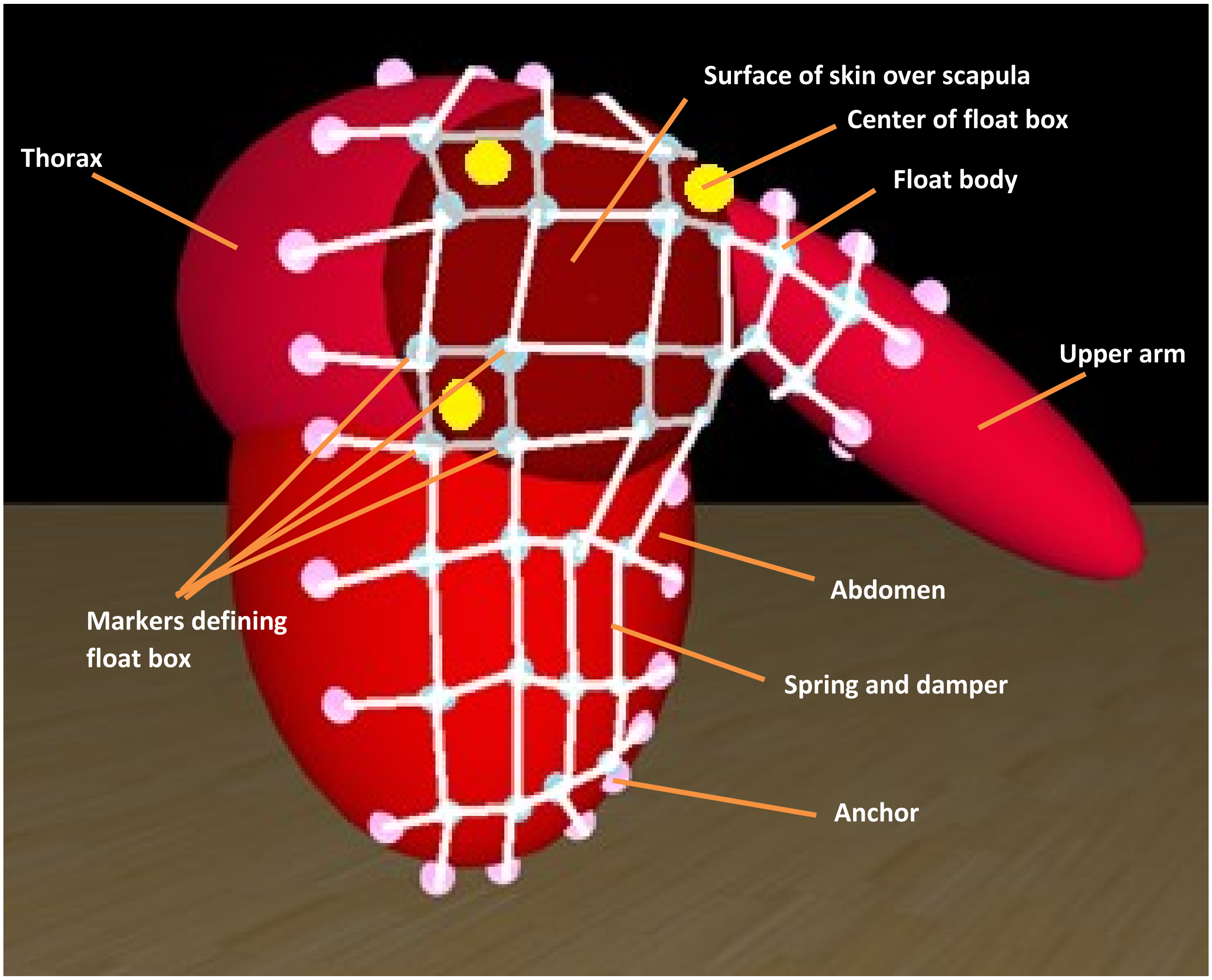

Figure 3.8: The proposed upper-extremity model. Ellipsoids approximate the shape of the skin covering the scapula (dark red) and the thorax, abdomen and upper arm (light red). Anchor bodies (pink) and float bodies (cyan) are constrained to move on the surfaces of these ellipsoids and are connected by springs and dampers (white and grey lines). The center-of-float-box (COFB) points (yellow) were tracked.

The anchors form a perimeter around the region in which the float bodies are placed, allowing the float bodies to move relative to each other and relative to the underlying bones as the bones move during the motion. Springs and dampers connect the float bodies to each other and connect the network of float bodies to the anchors. The springs and dampers are used to simulate the deformation of the skin, where the system is assumed to remain in static equilibrium (described below). The values for the spring and damper parameters were manually selected and tuned so that the springs' normalized lengths remain within a physiologically reasonable range. Dampers are required in the proposed model so that the system quickly reaches equilibrium during the dynamic simulations. On the scapula ellipsoid, four sets of four float bodies each were defined in a rectangular formation. The center of each of these boxes was used to represent the location of a skin-mounted marker. Each center-of-float-box (COFB) point moves during a simulation; these trajectories approximate those of the corresponding motion capture markers that are affixed to stretching, sliding skin during an experiment. The modelling and simulation processes are described in more detail below. All model-building, simulation, and analysis tasks were performed in Python using the OpenSim application programming interface (API).

Spring–damper system

Before the final model was built, several tests were performed to verify certain elements of the model. First, a nonlinear spring component was tested by attaching springs between several bodies in a straight line (see Figure 3.9) and observing whether the motion resembles human skin stretch. The test involved having two fixed markers at the ends of the line and three markers that can move along one axis, all attached to each other with springs and dampers. The positions of the moveable markers were changed and a dynamic settling simulation was run to observe the movement of the markers. The following equation was used to calculate the force generated by each spring–damper component when stretched (no force is generated when the spring is shorter than its slack length):

$$F = (k \cdot \Delta l^2) - cv \qquad (1)$$

where F is the force generated by the spring–damper, k is the spring constant, Δl is the displacement of the spring, c is the damping coefficient and v is the velocity of one end of the spring relative to the other.

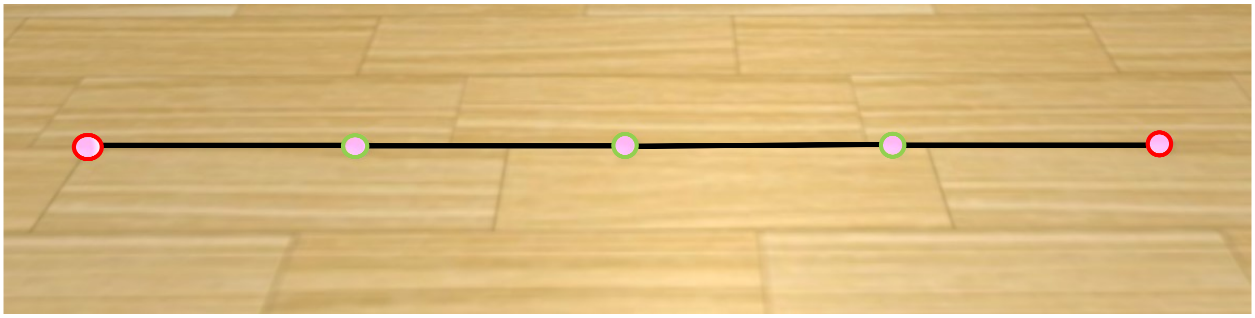

Figure 3.9: Spring test model. Pink circles with red outlines are bodies fixed to ground. Pink circles with green outlines are bodies that can translate along the horizontal axis. All black lines are springs and dampers of equal lengths and properties.

Equation (1) was applied to model all the spring–dampers in the model; however, the nonlinear springs were found to be generating very large forces during dynamic simulation tests and had non-physiological motion due to the squaring of the spring displacement (discussed in more detail later in this chapter). Thus, linear springs were used instead:

$$F = (k \cdot \Delta l) - cv \tag{2}$$

Using this equation led to more stable simulations, but it assumes that the skin remains in the linear region of the stress–strain curve. Other stress–strain curves could also be used, such as a piecewise linear relationship comprising a linear toe region followed by a second steeper linear region. However, given the large variability in skin stiffness between individuals [75], Eq. (2) was considered to be suitable for our proof-of-concept model.

Adding ellipsoids and markers

Before augmenting Seth's upper-extremity model, a simpler OpenSim model called "arm26" was used to test our modelling approach and algorithms (Figure 3.10). First, two ellipsoids were added to the arm26 model to represent the upper arm and the forearm. The size and shape of the ellipsoids were manually adjusted to fit on the model and to approximate the skin surface on each body segment.

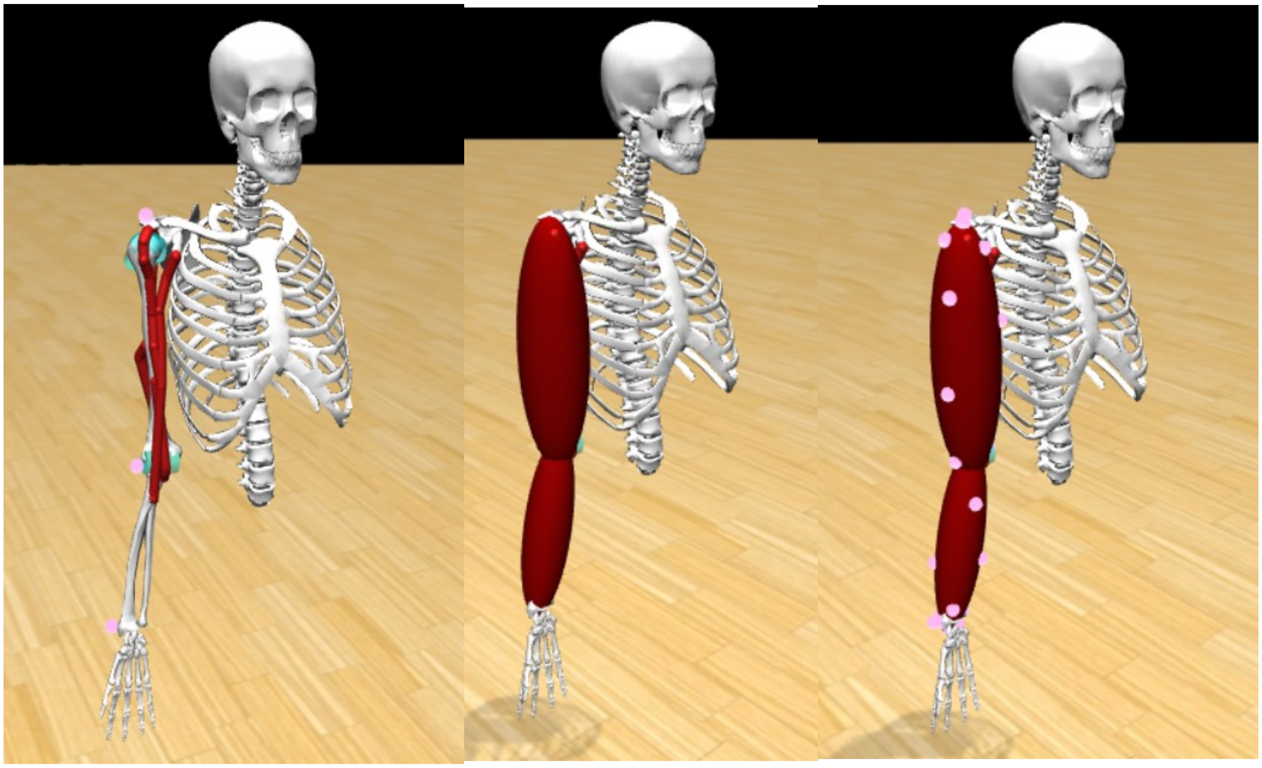

Figure 3.10: The original and modified "arm26" models. Left: the original model provided with OpenSim; center: the model with ellipsoids (red) added to the humerus and forearm body segments; right: the model with float bodies and markers (pink spheres) added. Spring–damper components are not shown.

Three algorithms were written in Python using the OpenSim API to create an intermediate model that was used to verify different aspects of the proposed model. Algorithm 1 was used to add the ellipsoids (through ellipsoid joints), float bodies, anchor bodies and markers to the arm26 model. In this "intermediate" model, the float bodies were constrained to move on the ellipsoids shown in Figure 3.10. The relationship between each float body and the underlying body segment (e.g., humerus) was defined by an ellipsoid joint. An ellipsoid joint is a concrete joint class in OpenSim that allows a child body to move on the surface of an ellipsoid attached to a parent body [76]. (The child body can also rotate about an axis perpendicular to the ellipsoid surface, but this degree of freedom was disregarded here since markers have no orientation.) Another algorithm (Algorithm 2) was used to evenly distribute the float bodies on the surface of the ellipsoids using magnet-like repulsive forces; this step was performed before adding the spring–damper components to help determine an appropriate rest length for each spring. A simulation of this "intermediate" model was run to ensure that (1) all of the float bodies were connected, (2) the float bodies reached equilibrium, and (3) the time needed to reach equilibrium was reasonable. The following equation (inspired by the equation for a magnetic repulsive force) was used for the repulsive force between pairs of bodies:

$$R = -\frac{0.1}{x^3} - cv \tag{3}$$

where R is the repulsive force generated, x is displacement, v is velocity and c is the damping coefficient. Damping is needed for the float bodies to settle during each dynamic simulation.

In the final step of the model setup phase, a third algorithm (Algorithm 3) was used to remove the "magnet-like" repulsive forces. This algorithm uses the final state of the intermediate model (i.e., the position of each float body after equilibrium has been reached) to create a new model that does not contain the repulsive forces. However, for the arm26 test model, an undeformed spring length of 10 cm was used for all springs. A more detailed description of each algorithm is provided below; pseudocode can be found in Appendix A.

Algorithm 1 – Add float bodies, anchor bodies and markers to a model

The inputs are an OpenSim model and a list of float bodies to be added onto each ellipsoid. The algorithm first adds ellipsoids to the model (with specified radii). The algorithm assigns random coordinate values to each float body, giving each float body a random location on the surface of the ellipsoid. The anchor bodies are then added to the thorax and humerus at specified locations.

Algorithm 2 – Add repulsive forces between all float bodies

The model produced by Algorithm 1 is used as an input for Algorithm 2. A list containing all float bodies in the model is used to define repulsive forces between each pair of float bodies.

Algorithm 3 – Create a new model without repulsive forces, and add springs and dampers

The model produced by Algorithm 2 is used as an input for Algorithm 3, after the float bodies have been evenly distributed by the repulsive forces (simply by running a dynamic simulation). Note that Algorithm 3 is used only for the “intermediate” model; the final skinned upper-extremity model is built using a slightly different procedure (described in the next section).

First, Algorithm 1 is used to create a new model without the repulsive forces added by Algorithm 2. The default value for all coordinates of the new model are set using the coordinate values from the input model. Each float body is then attached to the nearest three float bodies with spring equation (1), where *k* is set to 10 N/m, the spring's slack length is set to 10 cm and *c* is set to 2.0 N·s/m. The two nearest float bodies are then attached to each anchor body using the same equation and parameter values.

Algorithms 1 and 2 were also used to build the final upper-extremity model used in this study, with minor modifications (e.g., changing the number of markers and the shape of the ellipsoids, and importing a plugin to add the "scapulothoracic" joint developed by Seth et al. [72]). Anchor bodies were placed on the model manually and were rigidly attached to skeletal segments in the model using weld joints (a type of joint in OpenSim that prohibits motion between two bodies [77]).

After extending the arm26 model described above and obtaining the positions of the markers (position of float bodies at equilibrium), the skeletal joints were then locked and a dynamic simulation was run to allow the float bodies to settle to their equilibrium positions; this model configuration was then used as the default model pose. This procedure was then repeated at each time step of an arm flexion test movement—that is, the skeletal coordinates were set and a dynamic simulation was run to allow the synthetic skin (float bodies) to reach equilibrium. The "settled" float marker positions at the end of each of these dynamic simulations were stored as the predicted positions of optical markers on the subject's skin.

Skinned upper-extremity model

The process of extending Seth's upper-extremity model began with the addition of 4 ellipsoids, shown in Figure 3.11. This involved using Algorithm 1 (above) and Algorithm 4 (below); anchor bodies were added manually. Because the ellipsoids were welded to the bone frames, the ellipsoids move with the bones as the skeletal joint coordinates change; the float bodies and anchor bodies move along with the ellipsoids. Algorithm 2 was not used to build this model; instead, the configuration of the float bodies was configured manually. Specifically, after using Algorithm 1 to add ellipsoids (through ellipsoid joints), float bodies, anchor bodies and markers, the float bodies were moved manually to a configuration that would best represent skin stretching and sliding for the movement and experimental data of interest. Four float bodies were placed around each experimental marker on the scapula in the model's default pose. The trajectory of the center of each four-marker set simulated the movement of a skin-mounted marker. A Python script was used to add anchors where necessary to achieve the desired float body configuration. Algorithm 4 was used to attach manually specified pairs of bodies with springs and dampers. (Algorithm 3 would result in an uneven mesh of springs and dampers.) Each spring attaches two bodies (either attaching float to float or float to anchor), the slack length of which was set to be 2% shorter than the initial distance between the bodies to which it attaches, to model skin tension in a neutral pose. The distance between two bodies was determined by calculating the distance between their 3D positions in the ground reference frame.

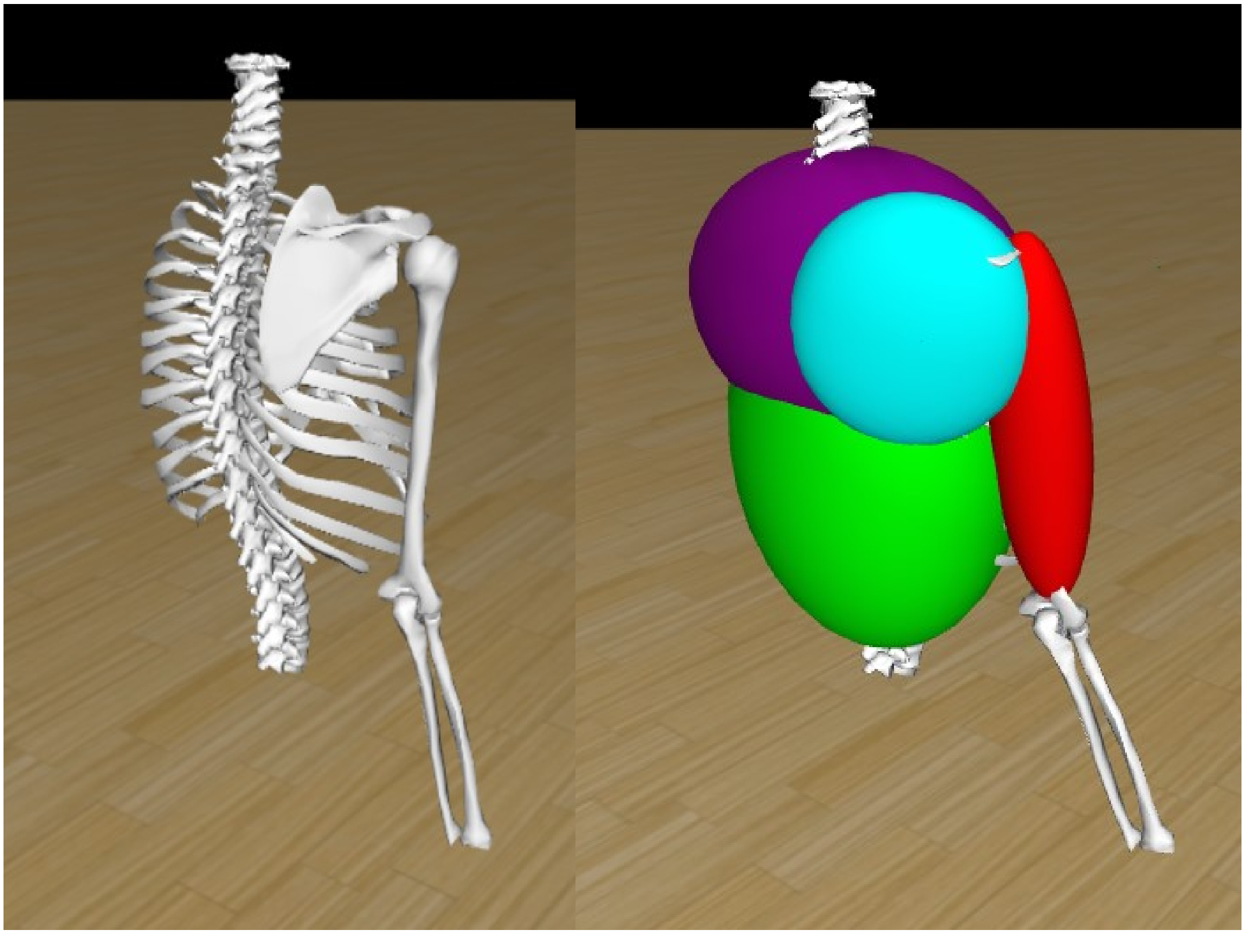

Figure 3.11: Seth's upper-extremity model [72] **(left) and the proposed model with ellipsoids added (right).** The purple ellipsoid represents the surface of the thorax, the green ellipsoid represents the abdomen, part of the blue ellipsoid represents the scapula skin plane, and the red ellipsoid represents the humerus body segment.

The final skinned upper-extremity model, shown in Figure 3.12, includes 4 ellipsoids representing the thorax, abdomen, upper arm and the scapula skin plane; 39 float bodies; 37 anchors on one side of the back; and 76 spring–damper components between float bodies and anchors. The center of each box of float markers ("center of float box" or COFB) is calculated and assumed to represent the location of a skin surface marker. The location of four float markers was averaged to reduce the sensitivity of the kinematic calculations to modelling parameters. Each float body has 4 attachments, some of which are to anchors and others are to other float bodies (see Figure 3.12A). In the initial design, the float bodies on the surface of the relatively flat scapula ellipsoid moved onto the side facing the thorax, which is physiologically impossible. Thus, the size of the scapula ellipsoid was increased (see Figure 3.12B) to prevent this from occurring and to increase the stability of the simulations. Although the scapula ellipsoid appears to be unreasonably large, note that the float bodies always reside within a relatively small region on its surface; only this region is used to approximate the surface of the skin.

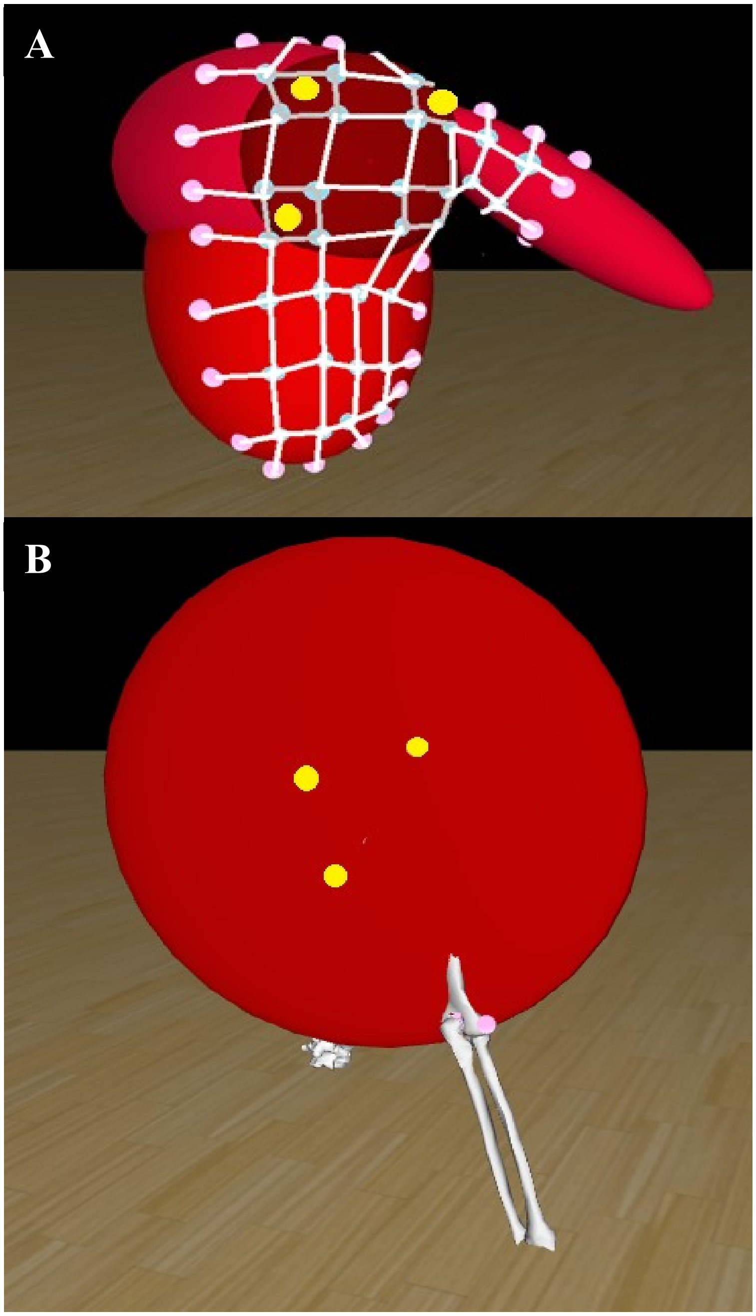

Figure 3.12: Arrangement of float bodies and spring–damper components in the final skinned upper-extremity model. (A) Initial design. Yellow circles are the model markers defined by Seth et al. [72], blue circles are the float bodies, pink circles are the anchor bodies, and white and grey lines are the spring–damper components. Grey lines indicate the float boxes whose centers (yellow circles) are tracked. (B) Model with enlarged scapula ellipsoid to better represent the surface of the skin covering the scapula (all other ellipsoids have been hidden in this image).

Algorithm 4 – Add spring-damper components between manually selected float bodies and anchor bodies

The input for this algorithm is the model with float and anchor bodies. For each pair of bodies to be connected with a spring–damper component, the distance l between the bodies is first computed. The spring's slack length is set to be 2% smaller than l—that is, $l_{\text{slack}} = 0.98l$. Variables l_{slack} and l are then used in Eq. (1) to define the force that is applied between the two bodies.

3.5 Simulation

This section discusses the simulation strategy that was used to estimate the model joint coordinates when simulating skin stretch, as summarized in Figure 3.13 below.

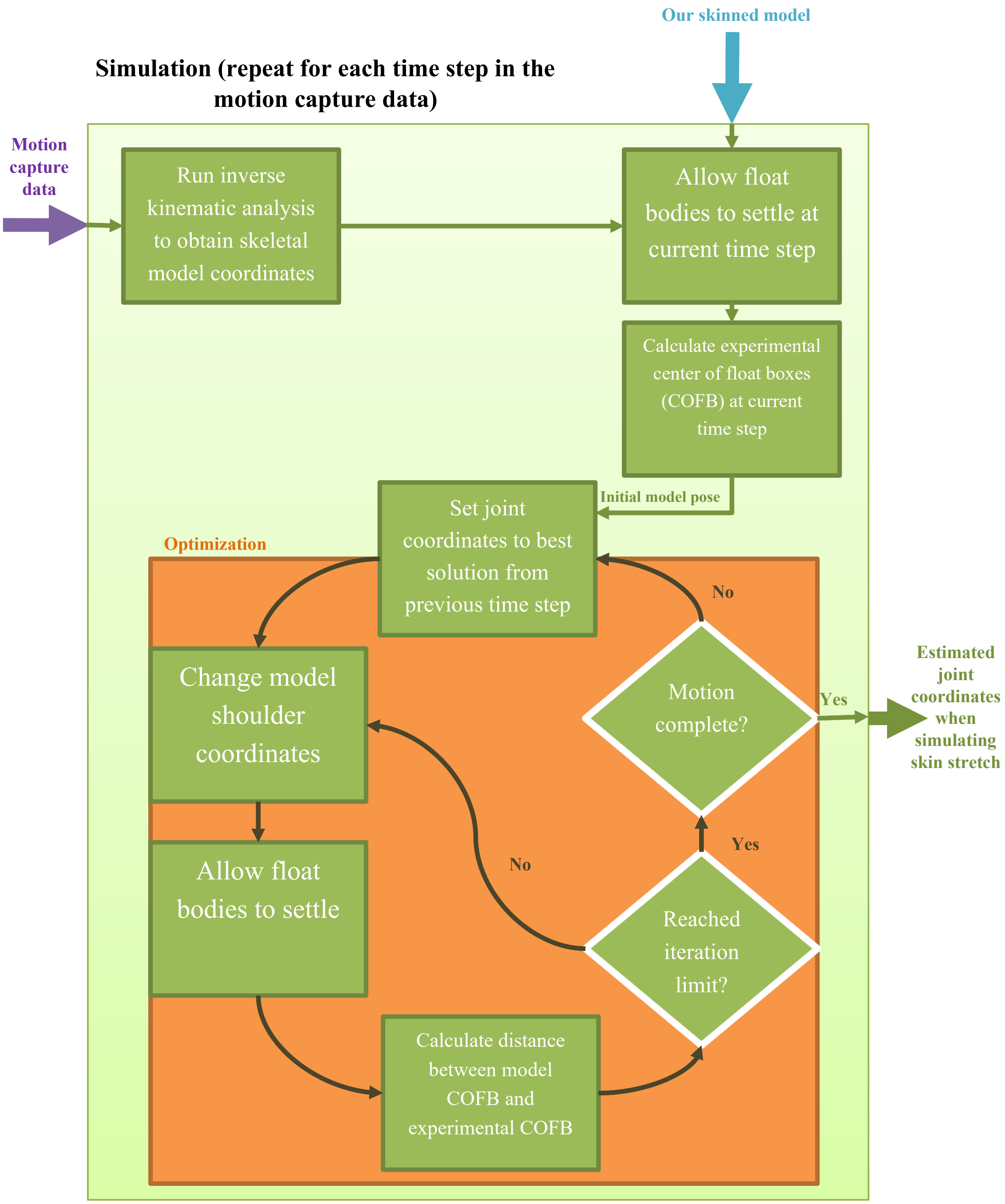

Figure 3.13: Simulation strategy used to estimate model joint coordinates taking skin stretch into account.

Synthetic skin markers

The synthetic skin markers present on the model are used in an optimization problem to estimate the joint coordinates throughout the abduction motion. In this process, OpenSim's InverseKinematicsSolver was used, which takes a set of model coordinate values and calculates a new set of coordinate values that respect the model constraints [78]. For this study, the InverseKinematicsSolver was used to take the optimizer-generated coordinate values (candidate solution) and calculate coordinate values that satisfy the model constraints. Seth et al. provided experimental joint coordinates in 0.1-second increments (shown in Figure 3.14) that were obtained by running inverse kinematics on the bone-pin measurements [72]. The movement (abducting the shoulder from the rest position) was simulated incrementally, where each of the model's coordinates was set to the values provided by Seth et al. at each time step. It is important to note that when the skeletal joint coordinates are changed, the bodies move to the new position instantaneously (along with the ellipsoids and their associated float bodies and anchor bodies). During this change, the springs and dampers do not produce any force; however, after the change, some springs will be longer and others will be shorter. Thus, when the dynamic settling simulation is started, the float bodies will move until a new equilibrium is reached. The skeletal joints were locked during the dynamic settling simulations, and the float bodies were allowed to settle for a maximum of 200 seconds. To reduce the simulation time, the simulation was performed in 20-second increments, stopping either when 200 seconds of simulation time had elapsed or when the maximum float body acceleration was less than a specified tolerance (suggesting that equilibrium had been reached). At the end of each dynamic settling simulation, the locations of the float bodies were stored. The COFB was then calculated for the three float boxes to generate synthetic skin marker trajectories (see Algorithm 6, below). Optionally, the COFB positions can be smoothed using a Savitzky-Golay filter in each axis independently (Algorithm 7), to evaluate the effect of experimental noise on the proposed simulation approach. The filter simulates noise by making changes in each coordinate direction to each COFB trajectory. An optimization strategy was used to obtain joint coordinates from the COFB trajectories (Algorithm 8).

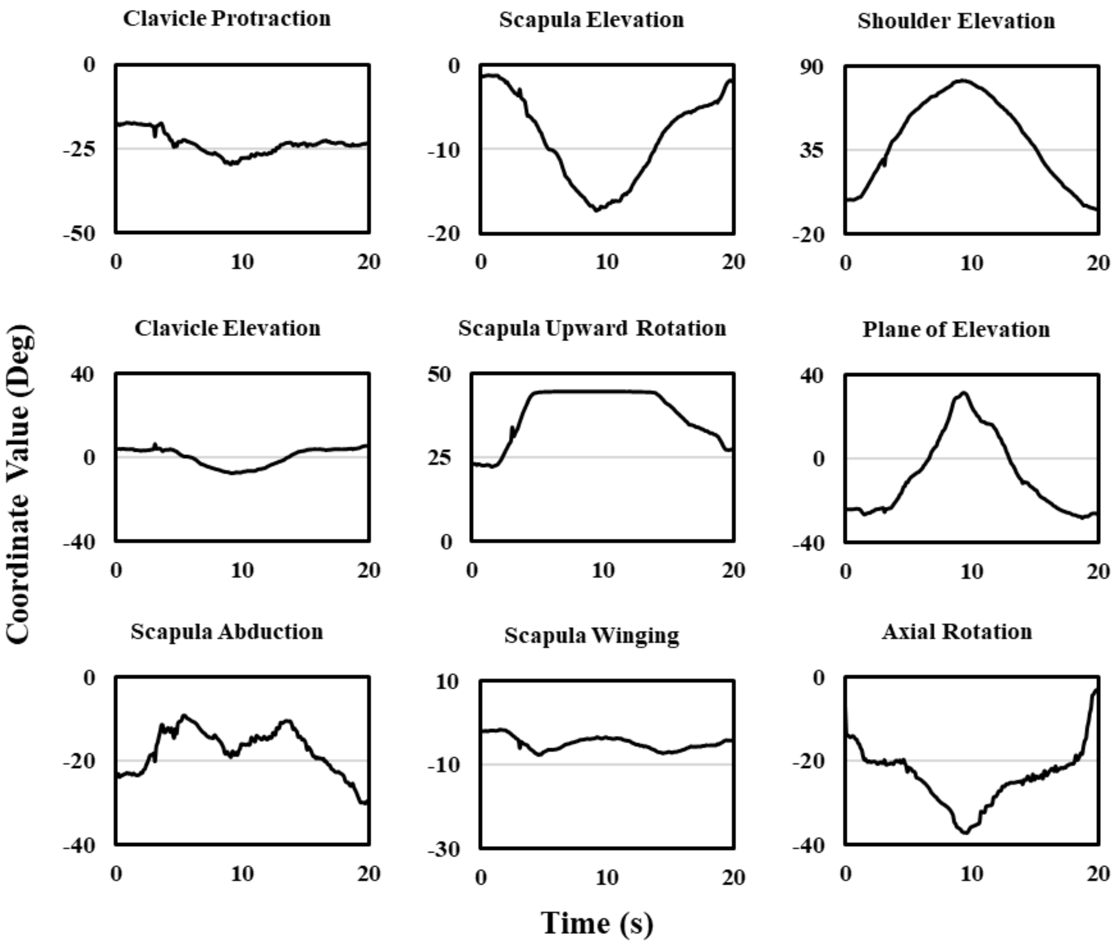

Figure 3.14: Model coordinate values obtained using bone pin markers. Black lines indicate the model coordinate values computed using experimental bone pin locations. Bone pin data were collected by Ludewig et al. [67].

Optimization

The covariance matrix adaptation evolutionary strategy (CMA-ES) optimization method was used to determine the joint coordinate values that minimize the error between the target and simulated skin marker positions. The CMA-ES method defines a mean and covariance from which a population of candidate solutions is selected; each of these candidate solutions is then tested. CMA-ES computes the mean and covariance for the next generation based on the relative fitness (objective function value) of the candidate solutions in the previous generation [20,79]. CMA-ES was chosen for this study because, unlike many other optimizers, it avoids converging to local optima [80].

Algorithm 5 – Calculate joint angles given the locations of synthetic skin makers on the skinned upper-extremity model

The input to this algorithm is the skinned upper-extremity model (Figure 3.12B) and the list of thorax coordinate values for each time step. The center-of-float-box (COFB) trajectories are calculated for the abduction motion (see Algorithm 6) and are stored in a list. Optionally, a filter is applied to the COFB trajectories (see Algorithm 7) to simulate noise. For each time step of the abduction motion, the thorax coordinates of the model are set and a CMA-ES optimization is performed to determine the shoulder joint coordinates that minimize the difference between the target and simulated COFB points (Algorithm 8). The model coordinates are then set to the solution from the optimizer (in preparation for the next time step of the abduction motion) and are stored for later plotting and analysis.

Algorithm 6 – Calculate center-of-float-box (COFB) trajectories

The input to this algorithm is a file containing the thorax and shoulder coordinate values over time, calculated from bone pin measurements. At each time step, the model thorax coordinates are set and the InverseKinematicsSolver is run using the corresponding shoulder coordinate values as the desired coordinate values. Upon refining the shoulder coordinate values (projecting onto the constraint manifold), the shoulder coordinates are locked and the float bodies are allowed to settle. The three COFBs are calculated and stored in a list. At the end of the algorithm, the list of COFB trajectories is saved to a file.

Algorithm 7 – Filter COFB trajectories

The input to this algorithm is the output file from Algorithm 6. The Savitzky-Golay filter is applied, separately, to each coordinate (X, Y, and Z) of each COFB trajectory over time. The results are saved to a file.

Algorithm 8 – CMA-ES optimization of the skinned upper-extremity model's joint coordinates at one time step

The inputs to this algorithm are the skinned upper-extremity model in its default pose and the file generated by Algorithm 6 containing the COFB locations computed from the experimental data.

Candidate solutions are generated, comprising values for each skeletal joint coordinate. The InverseKinematicsSolver is run for each candidate solution to ensure the skeletal coordinates describe a feasible model pose; the skeletal coordinates are locked in this pose for the duration of the corresponding dynamic simulation. The float bodies are then allowed to move in a dynamic settling simulation. The simulation is run incrementally until 200 seconds of simulated time have elapsed or the float bodies' acceleration is below a specified threshold (suggesting that equilibrium has been reached). At the end of each dynamic settling simulation, objective function J is calculated, where J is the sum of the distances between three pairs of model COFBs and experimental (target) COFBs.

4. Results and Discussion

This chapter presents simulation results that were generated using experimental data in which the shoulder was abducted from a rest position. The results from the initial model development are described first, then the results using the "skinned" upper-extremity model are presented. The model is verified by determining whether the mesh of float bodies is able to approximate skin stretch and sliding. This was done by observing the changes in the potential energies and lengths of the springs in the mesh. Finally, the optimization results are discussed, in which the added float bodies were used to estimate skeletal joint angles. The joint angle estimates were compared to the joint angles computed directly from bone pin data.

4.1 Verification of spring potential energies

It was assumed that the skin remains in static equilibrium during sufficiently slow movements. The average spring potential energy was calculated over the duration of the abduction movement (19.9 seconds) to ensure that all the springs had settled at an energy above zero (note that the springs do not generate or store force when compressed). This state indicates that the skin is under tension and the float bodies are no longer moving. The potential energy (PE) of each spring was calculated as follows:

$$PE = \frac{1}{2}k\Delta l^2 \tag{4}$$

where k is the spring constant and Δl is the stretch of the spring ($\Delta l = l - l_{\text{slack}}$). The force produced by a spring is set to zero when its length is less than its slack length (i.e., potential energy is zero if $\Delta l < 0$). The average PE of all springs was then calculated to monitor the average skin stretch as the arm is being raised. The average PE of all springs was computed at 0.01-second intervals during each 200-second dynamic settling simulation.

As shown in Figure 4.1, the average PE peaks at the beginning of each settling simulation, after the skeletal coordinates have changed, and then quickly decreases and settles after approximately 50 seconds of each 200-second interval. The initial location of the float bodies in each interval is the final equilibrium position from the previous interval. It can also be seen that the final average potential energy of the springs after stabilization changes throughout the motion. The peak rises in the centre of the graph because the springs change length instantaneously when the coordinates are changed. Since only the stretched springs generate force, the PE peaks at the start of each time step and decreases as the float body mesh moves to equilibrium. It is important to note that the spikes at the beginning of each time step are not meant to represent physiological skin movement. Only the final state of the model after the skin mesh has reached equilibrium is intended to represent the position of skin markers in that model pose. Furthermore, the height and width of the spikes will differ depending on the damping coefficient and the mass assigned to the markers, both of which are arbitrary but only affect the amount of time required for the skin to reach equilibrium (because, at equilibrium, velocities and accelerations are zero).

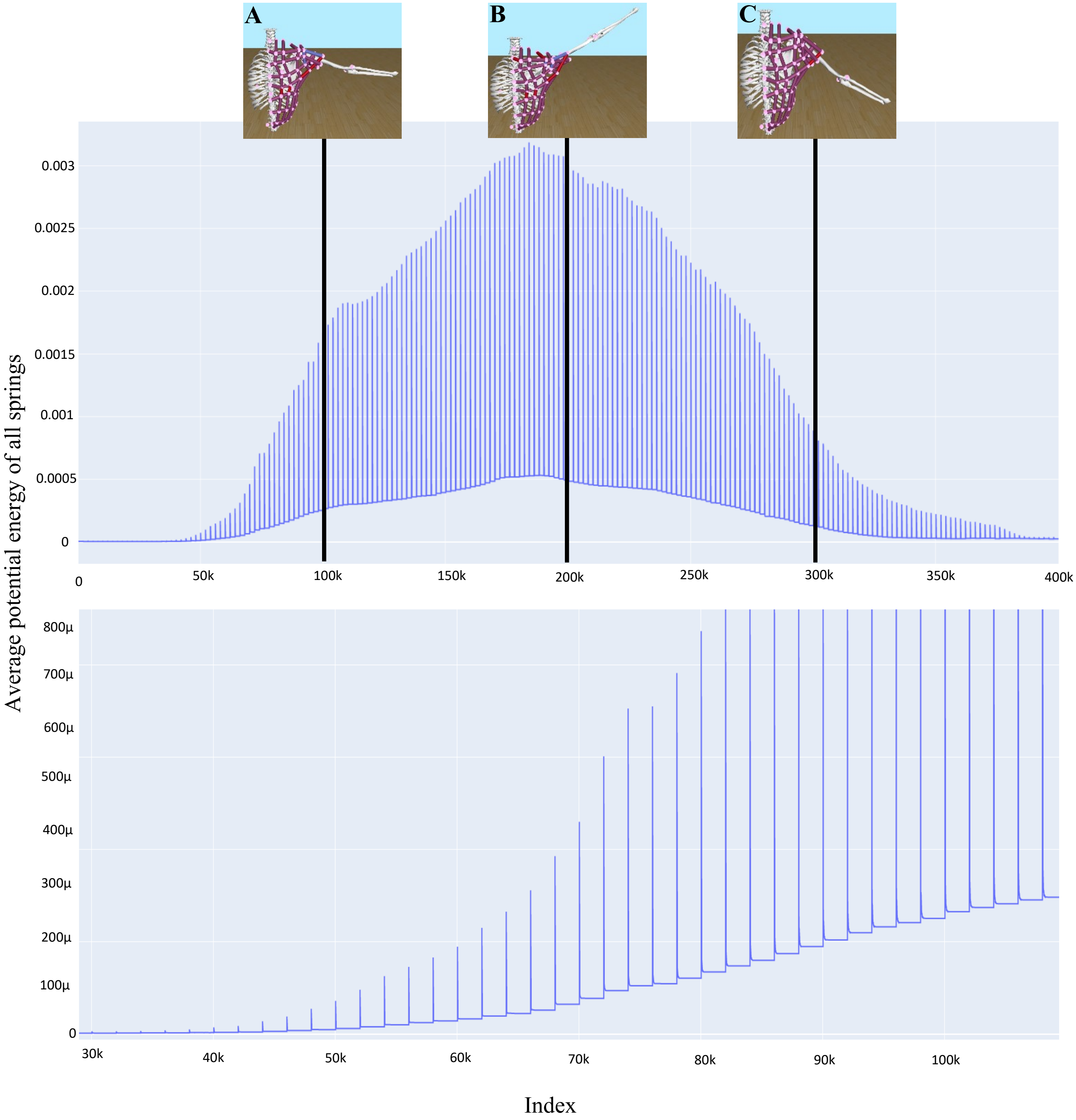

Figure 4.1: Average potential energy of springs over time. Top: all the points in each dynamic settling simulation have been assembled over all time steps of the abduction motion; bottom: the data corresponding to the interval between 4 seconds and 6.5 seconds of the motion. Images A, B and C are taken at 25%, 50% and 75% of the abduction motion, respectively.

4.2 Verification of spring lengths

To further verify the model, the length of each spring over time was examined to determine when the synthetic skin remained in tension. This analysis was also used to confirm that the springs had stabilized during each 200-second settling simulation. To facilitate this analysis, the length of each spring was normalized by its slack length (l_{slack}, the length at which it begins generating force). A spring whose normalized length is less than 1 indicates that the synthetic skin is slack in this region and direction. In total, there are 76 springs in the skinned upper-extremity model.

As shown in Figure 4.2, many springs reach equilibrium in each interval. Most springs stabilize at a normalized length between 0.8 and 1.3, with a few occasional outliers. The reason some springs settle below 0.8 or above 1.3 might be because springs that are closer to the shoulder undergo a greater change in length during the abduction motion compared to the springs that are closer to the spine. Further tuning of the model parameters may address this issue but is beyond the scope of the current study. Furthermore, some springs experience high-frequency vibrations indicating that the attached float bodies have not completely settled. This potential source of error is addressed in the optimization strategy (described in the next section).

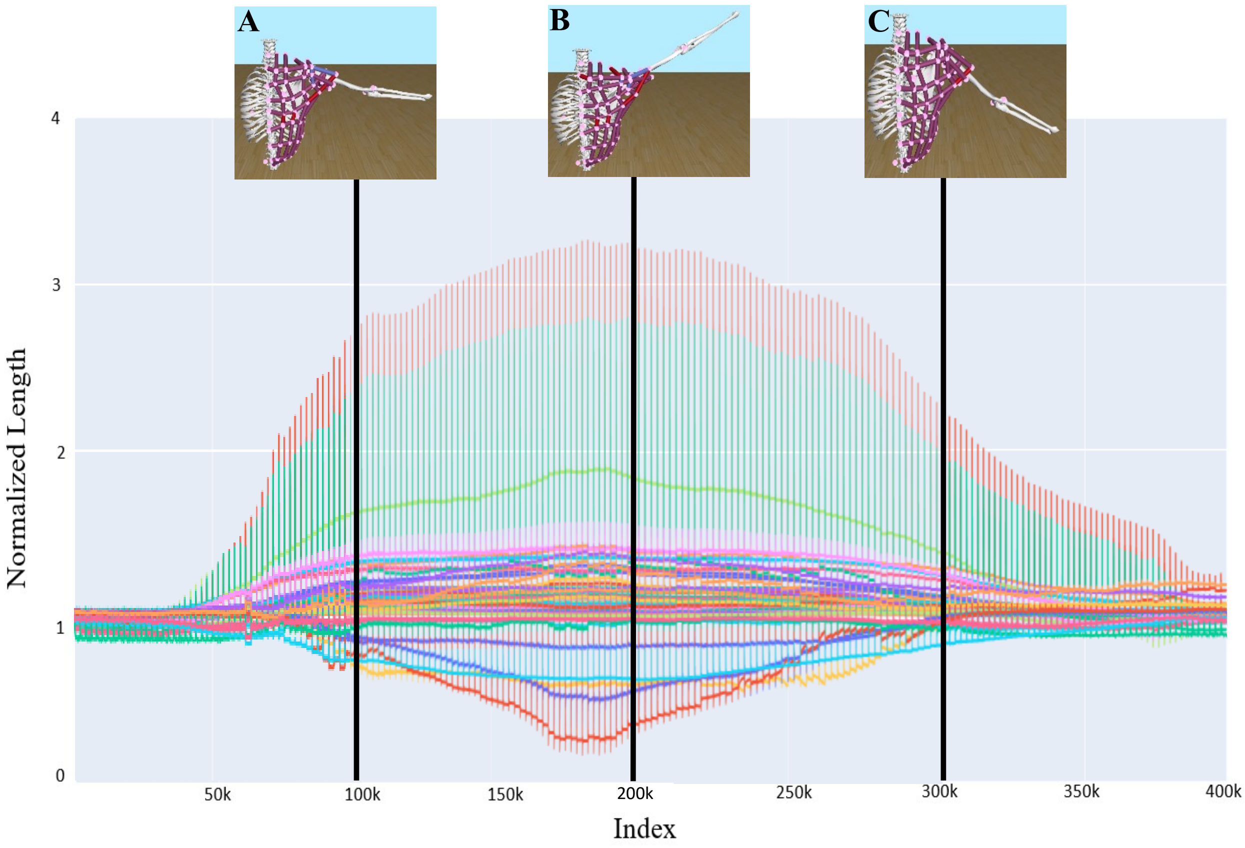

Figure 4.2: Normalized spring lengths over the abduction motion. The normalized lengths of all springs during each 200-second dynamic settling simulation are plotted over the entire movement.

4.3 Optimization

The optimization strategy that was used to simulate skin stretch in the “skinned” upper-extremity model is described in Section 3.6. Figure 4.3 shows the shoulder coordinates that were obtained from the optimization procedure and compares them with those obtained using inverse kinematics calculations from bone pin data. As shown, filtering the COFB trajectories independently along each axis led to worse results than the original, unfiltered trajectories. Because filtering the COFB locations in each dimension was done independently (i.e., treating the X, Y, and Z coordinates as independent signals), the resulting COFB locations can be either impossible to obtain through any combination of shoulder coordinates or associated with an entirely different shoulder configuration. Additionally, the accuracy of the obtained coordinate values varies between coordinates in both filtered and unfiltered scenarios. For example, clavicle protraction and shoulder elevation coordinate values generated from the unfiltered data closely matched those obtained from experimental bone pins; however, other coordinates such as scapula winging and axial rotation were substantially different from the values obtained from experimental bone pin data. The large difference in these coordinates may be due to COFBs that are close to the axis of the movement, meaning that a large change in the coordinate value would be required to move the COFB closer to the correct position. Theoretically, in the unfiltered scenario, the optimizer would have obtained the same coordinate values as those that were obtained from the bone pin data (i.e., the blue curves would have been overlapping the black curves in Figure 4.3) since the bone pin data were used to generate the synthetic skin marker trajectories. The difference between the black and blue curves may be attributed to the presence of multiple local minima in the objective function surface.

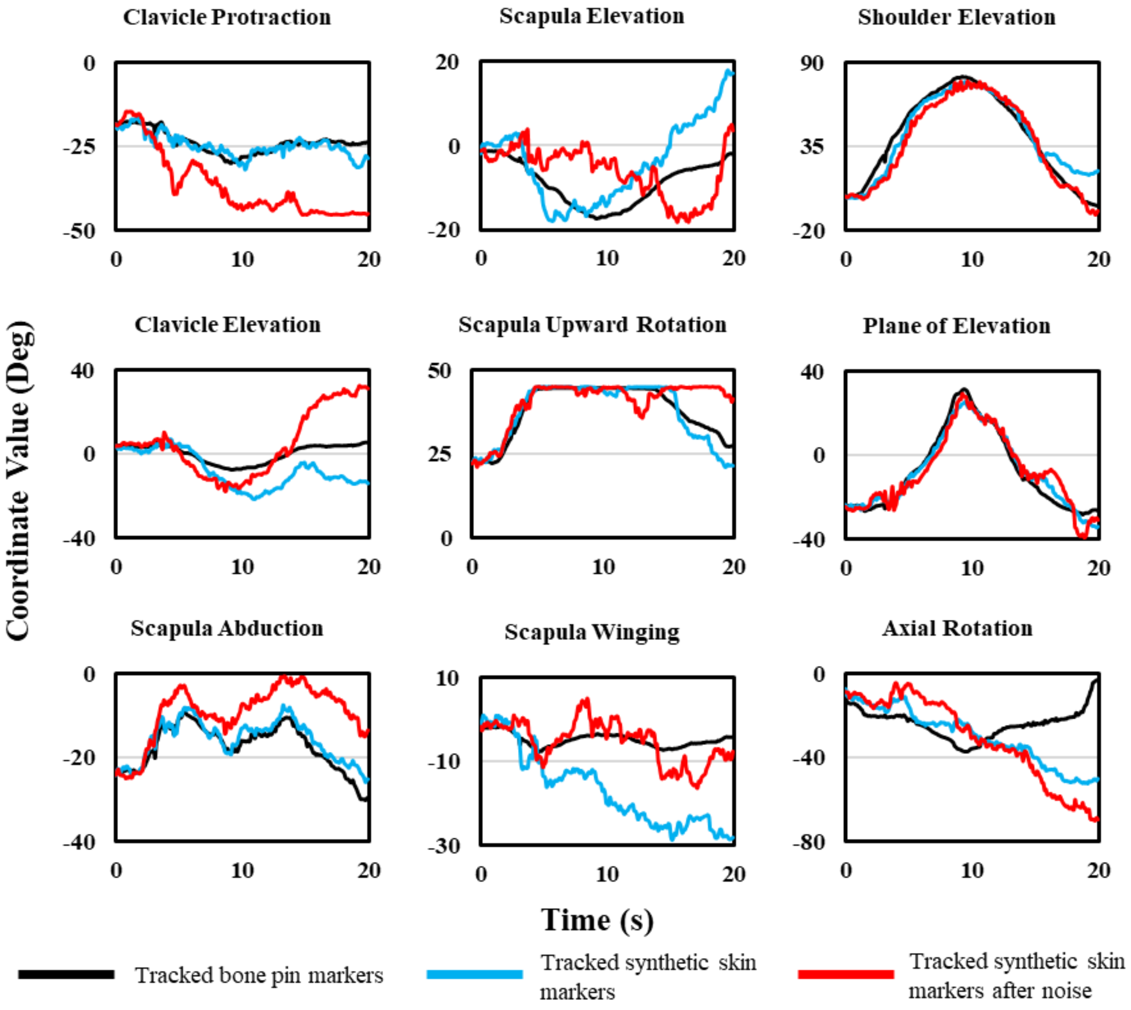

Figure 4.3: Model coordinate values obtained using bone pin markers and optimization. Black lines indicate the model coordinate values computed using experimental bone pin locations. Blue and red lines indicate the coordinate values obtained using optimization with unfiltered and filtered center-of-float-box trajectories, respectively.

The total execution time for the optimization (Algorithm 5) using unfiltered COFB trajectories was about 52.15 hours (2 days, 4 hours, 9 minutes), and the runtime using smoothed COFB trajectories was about 94.88 hours (3 days, 22 hours, 53 minutes). The difference in execution times may be due to differences in the number of integration time steps required by the dynamic settling simulations. Also note that the peak objective function value when using unfiltered COFB trajectories was approximately 2 mm; when using filtered COFB trajectories, the peak objective function value was approximately 6 mm (Figure 4.4). Furthermore, notice that the objective function value increases dramatically at the end of the movement when filtered COFB trajectories were used (the red line in Figure 4.4 beyond 160 seconds). These observations suggest an important conclusion: experimental measurements should not be filtered independently along each coordinate direction as this can destroy the spatial relationship among measured values.

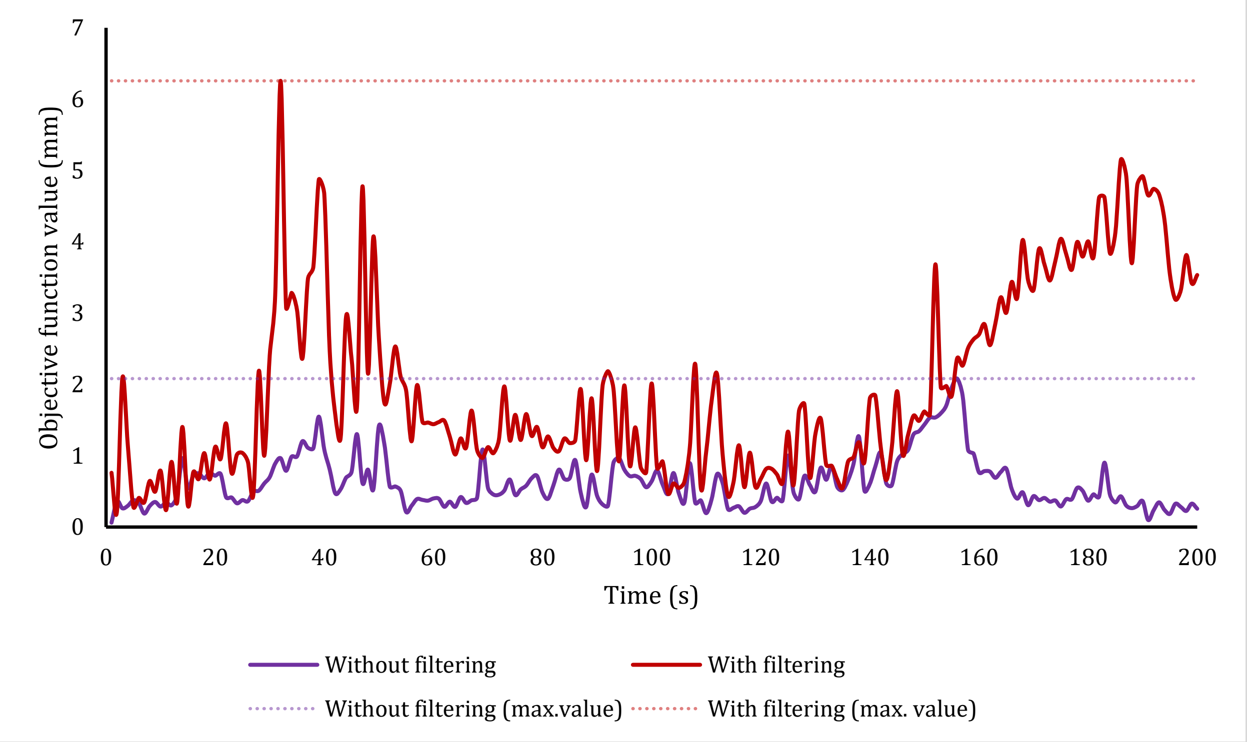

Figure 4.4: Objective function values obtained during the abduction motion. The objective function value is the sum of the distances between the three model COFB locations (found by the optimizer) and the corresponding experimental COFB locations (calculated using inverse kinematics with bone pin measurements). The objective function values obtained using the unfiltered COFB trajectories (purple) are substantially lower than those obtained using the filtered COFB trajectories (red).

4.4 Results comparison

The results indicate that the skinned upper-extremity model is capable of capturing several salient features of skin stretch and scapula sliding motion for a shoulder abduction movement. The model built by Seth et al. [72] reduced the effects of STA in inverse kinematics calculations substantially, simply by using a constrained kinematic model. Augmenting the model with synthetic skin may further reduce the effects of STA in practice, provided the parameters of the model can be appropriately determined. If the simulation time can be reduced, the proposed modelling approach may increase the feasibility of using inverse kinematics simulations in a clinical setting, which is currently limited by errors due to STA. As discussed earlier, simulating skin sliding and stretching could also be useful in studies involving movements with large amounts of STA, such as jumping. The final skin stretch motion can be seen in Figure 4.5.

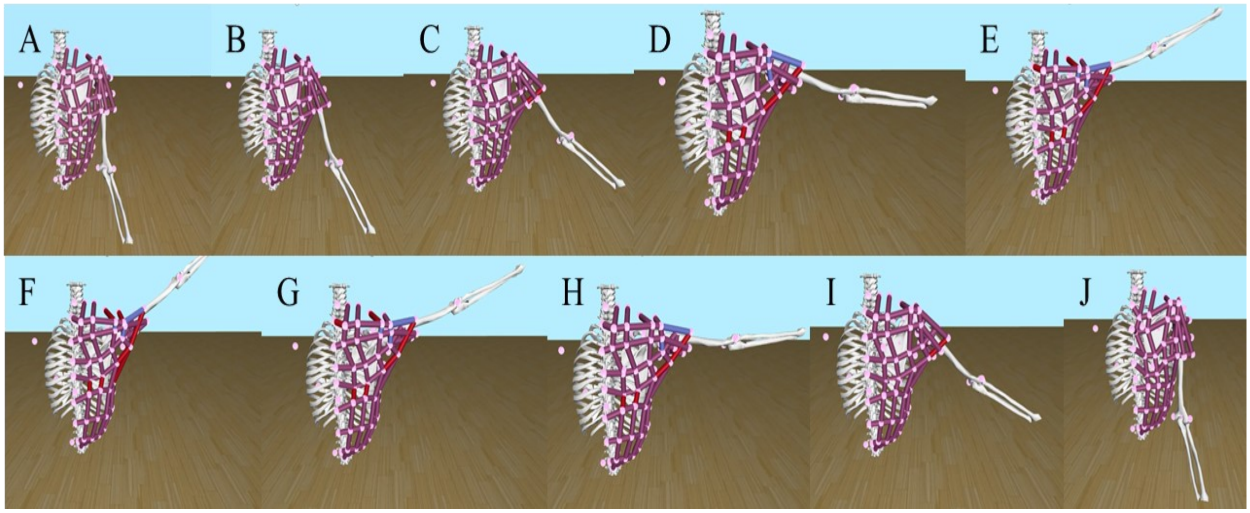

Figure 4.5: Pose of the skinned model throughout the abduction motion. Panels A–J show the motion in equal time increments from start to finish. Purple lines indicate springs with normalized length between 0.8 and 1.3. Red lines indicate springs with normalized length greater than 1.3 (large amount of stretch). Blue lines indicate springs with normalized length less than 0.8 (very loose).

The proposed modelling and simulation approach involved using a mesh of springs and dampers to approximate skin stretch during abduction of the shoulder. As can be seen above, the synthetic skin stretches and relaxes in a way that resembles real skin. For example, in panels C–I, the scapula slides under the mesh as the arm is raised. The red lines are present mainly in the latissimus dorsi area, which agrees with what is expected as the arm is raised during shoulder abduction. Additionally, blue lines are concentrated at the top of the humerus. This also agrees with what is expected as the skin at the top of the shoulder relaxes when the arm is abducted. During model development, it was verified that the float bodies settled at the end of each time step. Furthermore, COFB trajectories were filtered to simulate added noise and to explore how the proposed model would accommodate data that have been filtered in this way. The results of the optimizations indicate that the proposed approach produced reasonable coordinate values for most of the shoulder coordinates. Additionally, for some shoulder coordinates, results from the filtered COFB trajectories were very close to the results from the unfiltered COFB trajectories, suggesting that the model may produce accurate joint angles even if the experimental data are noisy. The objective function value from the optimization without filtering the COFB trajectories remained at a low value for the duration of the movement (on average, less than 1 mm error in each COFB location).

5. Conclusions

The proposed model produced promising results in simulating skin stretch and sliding in the shoulder during an abduction movement, and in computing several coordinate values given trajectories of points on the skin. Based on these results, it can be concluded that the strategy for simulating skin stretch that was used in this study has produced a mixed outcome. Most of the coordinate values obtained from bone pin data were closely reproduced using the skin stretch model; however, inaccurate results were obtained for three of the nine coordinates. This work represents an advance in the modelling of soft-tissue artifacts (STA) in OpenSim and could be used to improve inverse kinematics calculations in both research and clinical settings. Through further improvement and calibration, the model could potentially be used in other studies to mitigate the effects of STA and increase the accuracy of model calculations. However, more experimental data are required to adequately test the model. Furthermore, the model would need to be adjusted not only for each body segment but also for subjects with different BMI and skin mechanical properties (e.g., stiffness).

5.1 Limitations

There are several limitations to this study; listed here are seven limitations that are believed to have the most impact. Fist, the "skinned" upper-extremity model only considers movement from a single individual, which means that the model may not apply equally well to other individuals. More experimental data are needed to test the accuracy of the skin motion for different individuals and motions. It is expected that the spring stiffnesses would need to be adjusted according to each subject's skin stress–strain curves. Second, the number of float bodies present was limited by computational power; increasing the number of float bodies on each body segment and anchor bodies around the perimeter may lead to more accurate results. Third, the anchor bodies were placed where the skin was assumed to be stationary during the motion; how the anchor body placement affects the results has not been investigated. Fourth, the optimization time required was just over two days, which may limit the utility of this method in practice and in other research studies. Fifth, the assumption that the springs always remain in the linear region of the skin stress–strain curve during the abduction motion may not be true. Sixth, the optimizer failed to achieve accurate results for some coordinates in the model, which may be due to the complexity of the model that was used or due to many local minimal that are inherent to the problem. Finally, using synthetic skin marker data proved useful in analyzing the results; however, it is not known whether using experimental skin marker data would produce similar results.

5.2 Future work

Due to time constraints and a lack of available experimental data, experimental validation of the model was not performed. Further analysis is needed by comparing the behaviour of the skin mesh to in-vivo human skin behaviour, which can be done by placing skin markers on a subject and comparing their movement to that of their model counterparts. The mechanical properties of the subject's skin should be measured and used to adjust the parameters of the model.

The results of this study could be extended in several ways. First, the simulations could be repeated with a larger number of float bodies and anchors to investigate how the number of float bodies affects the accuracy of the results. Second, the optimization strategy could be improved (using a different optimizer, for example) to reduce execution time, increasing the feasibility of using this model in other studies. For example, by removing the dampers and the masses of the float bodies, a determinate solution can be obtained by solving the linear system $F=KX$ and inverting the K matrix to obtain the spring displacements X. Third, the model could be further modified to include the effects of muscle bulging on the locations of skin markers. Such a model could involve dynamically changing the radii of the ellipsoids based on the computed activity of the underlying muscles. Fourth, the model could be applied to data from more subjects and movements to understand which model parameters are most important in producing accurate results. Finally, the model could be used to test low- and high-impact motions such as walking and running to determine how the intensity of the exercise (accelerations) affects the accuracy of the "skinned" model predictions. Considering the dynamics of skin motion (i.e. removing the assumption that it remains in equilibrium) may be necessary to produce accurate results in high-impact motions.

References

[1] Lu, T. W., and Chang, C. F., 2012, "Biomechanics of Human Movement and Its Clinical Applications," Kaohsiung J. Med. Sci., **28**(2), pp. S13–S25.

[2] Blair, D. J., Barg, A., Foreman, K. B., Anderson, A. E., and Lenz, A. L., 2020, "Methodology for Measurement of in Vivo Tibiotalar Kinematics After Total Ankle Replacement Using Dual Fluoroscopy," Front. Bioeng. Biotechnol., **8**, p. 375.

[3] Malleson, C., Collomosse, J., and Hilton, A., 2020, "Real-Time Multi-Person Motion Capture from Multi-View Video and IMUs," Int. J. Comput. Vis., **128**(6), pp. 1594–1611.

[4] Miranda, D. L., Rainbow, M. J., Crisco, J. J., and Fleming, B. C., 2013, "Kinematic Differences between Optical Motion Capture and Biplanar Videoradiography during a Jump-Cut Maneuver," J. Biomech., **46**(3), pp. 567–573.

[5] Miranda, D. L., Fadale, P. D., Hulstyn, M. J., Shalvoy, R. M., Machan, J. T., and Fleming, B. C., 2013, "Knee Biomechanics during a Jump-Cut Maneuver: Effects of Sex and ACL Surgery," Med. Sci. Sports Exerc., **45**(5), pp. 942–951.

[6] Rajt'úková, V., Michalíková, M., Bednarcíková, L., Balogová, A., and Živčák, J., 2014, "Biomechanics of Lower Limb Prostheses," Procedia Engineering, pp. 382–391.

[7] Mayo Clinic, 2019, "Plantar Fasciitis" [Online]. Available: https://www.mayoclinic.org/diseases-conditions/plantar-fasciitis/symptoms-causes/syc-20354846. Accessed on 17 May 2021.

[8] Moyne-Bressand, S., Dhieux, C., Dousset, E., and Decherchi, P., 2018, "Effectiveness of Foot Biomechanical Orthoses to Relieve Patients Suffering from Plantar Fasciitis: Is the

Reduction of Pain Related to Change in Neural Strategy?," Biomed Res. Int., **2018**, p. 3594150.

[9] Kim, S. H., Ahn, S. H., Jung, G. S., Kim, J. H., and Cho, Y. W., 2016, "The Effects of Biomechanical Foot Orthoses on the Gait Patterns of Patients with Malalignment Syndrome as Determined by Three Dimensional Gait Analysis," J. Phys. Ther. Sci., **28**(4), pp. 1188–1193.

[10] Herr, H., 2009, "Exoskeletons and Orthoses: Classification, Design Challenges and Future Directions," J. Neuroeng. Rehabil., **6**, p. 21.

[11] Chang, S. R., Nandor, M. J., Li, L., Kobetic, R., Foglyano, K. M., Schnellenberger, J. R., Audu, M. L., Pinault, G., Quinn, R. D., and Triolo, R. J., 2017, "A Muscle-Driven Approach to Restore Stepping with an Exoskeleton for Individuals with Paraplegia," J. Neuroeng. Rehabil., **14**, p. 48.

[12] Chang, S. R., Kobetic, R., Audu, M. L., Quinn, R. D., and Triolo, R. J., 2015, "Powered Lower-Limb Exoskeletons to Restore Gait for Individuals with Paraplegia - a Review," Case Orthop. J., **12**(1), pp. 75–80.

[13] Li, L., 2012, "How Can Sport Biomechanics Contribute to the Advance of World Record and Best Athletic Performance?," Meas. Phys. Educ. Exerc. Sci., **16**(3), pp. 194–202.

[14] McMahon, T. A., and Greene, P. R., 1978, "Fast Running Tracks," Sci. Am., **239**(6), pp. 148–163.

[15] López, M. C., Arias, J. L., Marín, P. G., and Yuste, J. L., 2014, "Time-Motion Analysis Procedure in Team Sports: Example for Youth Basketball," Strength Cond. J., **36**(3), pp.

71–75.

[16] Garg, A., and Kapellusch, J. M., 2009, “Applications of Biomechanics for Prevention of Work-Related Musculoskeletal Disorders,” Ergonomics, **52**(1), pp. 36–59.

[17] Kulig, K., and Burnfield, J. M., 2008, “The Role of Biomechanics in Orthopedic and Neurological Rehabilitation,” Acta Bioeng. Biomech., **10**(2), pp. 3–14.

[18] Mueller, M. J., Smith, K. E., Commean, P. K., Robertson, D. D., and Johnson, J. E., 1999, “Use of Computed Tomography and Plantar Pressure Measurement for Management of Neuropathic Ulcers in Patients with Diabetes,” Phys. Ther., **79**(3), pp. 296–307.

[19] An, K. N., 1984, “Kinematic Analysis of Human Movement,” Ann. Biomed. Eng., **12**(6), pp. 585–597.

[20] Uchida, T. K., and Delp, S. L., 2020, *Biomechanics of Movement: The Science of Sports, Robotics, and Rehabilitation*, Cambridge, MA: MIT Press.

[21] Washington University Orthopedics, 2017, “The Anatomy of the Elbow,” [Online]. Available: https://www.ortho.wustl.edu/content/Patient-Care/3151/Services/Shoulder-Elbow/Overview/Elbow-Arthroscopy-Information/The-Anatomy-of-the-Elbow.aspx. Accessed on 17 May 2021.

[22] Ren, L., Qian, Z., and Ren, L., 2014, “Biomechanics of Musculoskeletal System and Its Biomimetic Implications: A Review,” J. Bionic Eng., **11**(2), pp. 159–175.

[23] Terry, G. C., and Chopp, T. M., 2000, “Functional Anatomy of the Shoulder,” J. Athl. Train., **35**(3), pp. 248–255.

[24] Novak, D., 2019, “Guide to Shoulder Anatomy” [Online]. Available: https://www.sports-

health.com/sports-injuries/shoulder-injuries/guide-shoulder-anatomy. Accessed on 17 May 2021.

[25] Billette, J., and Janz, T., 2011, "Injuries in Canada : Insights from the Canadian Community Health Survey," Stat. Canada Cat. Publication no. 82-624-X.

[26] Watson, L. R., Turley, R., Joseph, T. N., 2021,"Common Injuries of theShoulder" [Online]. Available: https://www.urmc.rochester.edu/encyclopedia/content.aspx?contenttypeid=1&contentid=832. Accessed on 17 May 2021.

[27] Pogorzelski, J., Fritz, E. M., Godin, J. A., Imhoff, A. B., and Millett, P. J., 2018, "Nonoperative Treatment of Five Common Shoulder Injuries: A Critical Analysis," Obere Extrem., **13**(2), pp. 89–97.

[28] Chiari, L., Della Croce, U., Leardini, A., and Cappozzo, A., 2005, "Human Movement Analysis Using Stereophotogrammetry. Part 2: Instrumental Errors," Gait Posture, **21**(2), pp. 197–211.

[29] Cappozzo, A., Della Croce, U., Leardini, A., and Chiari, L., 2005, "Human Movement Analysis Using Stereophotogrammetry. Part 1: Theoretical Background," Gait Posture, **21**(2), pp. 186–196.

[30] O'Reilly, M., Caulfield, B., Ward, T., Johnston, W., and Doherty, C., 2018, "Wearable Inertial Sensor Systems for Lower Limb Exercise Detection and Evaluation: A Systematic Review," Sport. Med., **48**(5), pp. 1221–1246.

[31] Ramsey, D. K., Wretenberg, P. F., Németh, G., Benoit, D. L., and Lamontagne, M., 2003,

"Methodological Concerns Using Intra-Cortical Pins to Measure Tibiofemoral Kinematics," Knee Surgery Sport. Traumatol. Arthrosc., **11**(5), pp. 344–349.

[32] Stagni, R., Fantozzi, S., Cappello, A., and Leardini, A., 2005, "Quantification of Soft Tissue Artefact in Motion Analysis by Combining 3D Fluoroscopy and Stereophotogrammetry: A Study on Two Subjects," Clin. Biomech., **20**(3), pp. 320–329.

[33] List, R., Postolka, B., Schütz, P., Hitz, M., Schwilch, P., Gerber, H., Ferguson, S. J., and Taylor, W. R., 2017, "A Moving Fluoroscope to Capture Tibiofemoral Kinematics during Complete Cycles of Free Level and Downhill Walking as Well as Stair Descent," PLoS One, **12**(10), p. e018952.

[34] Young, P., Rhea, E., Rasmussen, L., and Loveless, E., 2019, "Biplanar Fluoroscopy in Pediatric Orthopaedics," Tech. Orthop. doi: 10.1097/BTO.0000000000000424

[35] Westberry, D. E., Davids, J. R., Cross, A., Tanner, S. L., and Blackhurst, D. W., 2008, "Simultaneous Biplanar Fluoroscopy for the Surgical Treatment of Slipped Capital Femoral Epiphysis," J. Pediatr. Orthop., **28**(1), pp. 43–48.

[36] Tsai, T. Y., Li, J. S., Wang, S., Lin, H., Malchau, H., Li, G., Rubash, H., and Kwon, Y. M., 2013, "A Novel Dual Fluoroscopic Imaging Method for Determination of THA Kinematics: In-Vitro and in-Vivo Study," J. Biomech., **46**(7), pp. 1300–1304.

[37] Mahfouz, M. R., Hoff, W. A., Komistek, R. D., and Dennis, D. A., 2003, "A Robust Method for Registration of Three-Dimensional Knee Implant Models to Two-Dimensional Fluoroscopy Images," IEEE Trans. Med. Imaging, **22**(12), pp. 1561–1574.

[38] Beckham, G., Suchomel, T., and Mizuguchi, S., 2014, "Force Plate Use in Performance

Monitoring and Sport Science Testing," New Stud. Athl., **29**(3), pp. 25–37.

[39] MSC Software, 2020, "ADAMS" [Online]. Available: https://www.mscsoftware.com/product/adams. Accessed on 17 May 2021.

[40] MSC Software, 2020, "MSC Software's Adams Used in Musculoskeletal Models That Simultaneously Predict Knee Loading and Muscle Forces during Movement" [Online]. Available: https://www.mscsoftware.com/academic-case-studies/msc-softwares-adams-used-musculoskeletal-models-simultaneously-predict-knee. Accessed on 17 May 2021.

[41] Marras, W. S., Knapik, G. G., and Ferguson, S., 2009, "Lumbar Spine Forces during Manoeuvring of Ceiling-Based and Floor-Based Patient Transfer Devices," Ergonomics, **52**(3), pp. 384–397.

[42] LIFEMODELER, 2020, "LifeMOD" [Online]. Available: http://www.lifemodeler.com/products/lifemod/. Accessed on 17 May 2021.

[43] Delp, S. L., Anderson, F. C., Arnold, A. S., Loan, P., Habib, A., John, C. T., Guendelman, E., and Thelen, D. G., 2007, "OpenSim: Open-Source Software to Create and Analyze Dynamic Simulations of Movement," IEEE Trans. Biomed. Eng., **54**(11), pp. 1940–1950. Accessed on 17 May 2021.

[44] Seth, A., Hicks, J. L., Uchida, T. K., Habib, A., Dembia, C. L., Dunne, J. J., Ong, C. F., DeMers, M. S., Rajagopal, A., Millard, M., Hamner, S. R., Arnold, E. M., Yong, J. R., Lakshmikanth, S. K., Sherman, M. A., Ku, J. P., and Delp, S. L., 2018, "OpenSim: Simulating Musculoskeletal Dynamics and Neuromuscular Control to Study Human and Animal Movement," PLoS Comput. Biol., **14**(7), p. e1006223.

[45] Dorn, T. W., Wang, J. M., Hicks, J. L., and Delp, S. L., 2015, "Predictive Simulation Generates Human Adaptations during Loaded and Inclined Walking," PLoS One, **10**(4), p. e0121407.

[46] Standford University, 2017, "Using Plugins," pp. 277–285 [Online]. Available: https://simtk-confluence.stanford.edu/display/OpenSim/Using+Plugins. Accessed on 17 May 2021.

[47] Lerner, Z. F., Gadomski, B. C., Ipson, A. K., Haussler, K. K., Puttlitz, C. M., and Browning, R. C., 2015, "Modulating Tibiofemoral Contact Force in the Sheep Hind Limb via Treadmill Walking: Predictions from an OpenSim Musculoskeletal Model," J. Orthop. Res., **33**(8), pp. 1128–1133.

[48] Rankin, J. W., Rubenson, J., and Hutchinson, J. R., 2016, "Inferring Muscle Functional Roles of the Ostrich Pelvic Limb during Walking and Running Using Computer Optimization," J. R. Soc. Interface, **13**(118), p. 20160035.

[49] Uchida, T. K., Seth, A., Pouya, S., Dembia, C. L., Hicks, J. L., and Delp, S. L., 2016, "Simulating Ideal Assistive Devices to Reduce the Metabolic Cost of Running," PLoS One, **11**(9), p. e0163417.

[50] Dembia, C. L., Silder, A., Uchida, T. K., Hicks, J. L., and Delp, S. L., 2017, "Simulating Ideal Assistive Devices to Reduce the Metabolic Cost of Walking with Heavy Loads," PLoS One, **12**(7), p. e0180320.

[51] Homayouni, T., Underwood, K. N., Beyer, K. C., Martin, E. R., Allan, C. H., and Balasubramanian, R., 2015, "Modeling Implantable Passive Mechanisms for Modifying the Transmission of Forces and Movements between Muscle and Tendons," IEEE Trans.

Biomed. Eng., **62**(9), pp. 2208–2214.

[52] DeMers, M. S., Hicks, J. L., and Delp, S. L., 2017, "Preparatory Co-Activation of the Ankle Muscles May Prevent Ankle Inversion Injuries," J. Biomech., **52**, pp. 17–23.

[53] Langholz, J. B., Westman, G., and Karlsteen, M., 2016, "Musculoskeletal Modelling in Sports-Evaluation of Different Software Tools with Focus on Swimming," Procedia Engineering, **147**, pp. 281–287.

[54] Barcaui, E. de O., Carvalho, A. C. P., Piñeiro-Maceira, J., Barcaui, C. B., and Moraes, H., 2015, "Study of the Skin Anatomy with High-Frequency (22 MHz) Ultrasonography and Histological Correlation," Radiol. Bras., **48**(5), pp. 324–329. doi: 10.1590/0100-3984.2014.0028.

[55] Benítez, J. M., and Montáns, F. J., 2017, "The Mechanical Behavior of Skin: Structures and Models for the Finite Element Analysis," Comput. Struct., **190**, pp. 75–107.

[56] Joodaki, H., and Panzer, M. B., 2018, "Skin Mechanical Properties and Modeling: A Review," Proc. Inst. Mech. Eng. Part H J. Eng. Med., **232**(4), pp. 323–343.

[57] Ní Annaidh, A., Bruyère, K., Destrade, M., Gilchrist, M. D., and Otténio, M., 2012, "Characterization of the Anisotropic Mechanical Properties of Excised Human Skin," J. Mech. Behav. Biomed. Mater., **5**(1), pp. 139–148.

[58] Paul, S. P., 2018, "Biodynamic Excisional Skin Tension Lines for Surgical Excisions: Untangling the Science," Ann. R. Coll. Surg. Engl., **100**(4), pp. 330–337.

[59] Abyaneh, M. A. Y., Griffith, R., Falto-Aizpurua, L., and Nouri, K., 2014, "Famous Lines in History: Langer Lines," JAMA Dermatology, **150**(10), p. 1087.

[60] Karla, A., Lowe, A., and Al-Jumaily, AM., 2016, “Mechanical Behaviour of Skin: A Review,” J. Mater. Sci. Eng., **5**(4), p. 1000254.

[61] Van Kuilenburg, J., Masen, M. A., and Van Der Heide, E., 2013, “Contact Modelling of Human Skin: What Value to Use for the Modulus of Elasticity?,” Proc. Inst. Mech. Eng. Part J J. Eng. Tribol., **227**(4), pp. 349–361.

[62] Fiorentino, N. M., Atkins, P. R., Kutschke, M. J., Goebel, J. M., Foreman, K. B., and Anderson, A. E., 2017, “Soft Tissue Artifact Causes Significant Errors in the Calculation of Joint Angles and Range of Motion at the Hip,” Gait Posture, **55**, pp. 184–190.

[63] Bourne, D., Choo, A., Regan, W., MacIntyre, D., and Oxland, T., 2009, “Accuracy of Digitization of Bony Landmarks for Measuring Change in Scapular Attitude,” Proc. Inst. Mech. Eng. Part H J. Eng. Med., **223**(3), pp. 349–361.

[64] Leardini, A., Chiari, A., Della Croce, U., and Cappozzo, A., 2005, “Human Movement Analysis Using Stereophotogrammetry Part 3. Soft Tissue Artifact Assessment and Compensation,” Gait Posture, **21**(2), pp. 212–225.

[65] Clément, J., Dumas, R., Hagemeister, N., and de Guise, J. A., 2015, “Soft Tissue Artifact Compensation in Knee Kinematics by Multi-Body Optimization: Performance of Subject-Specific Knee Joint Models,” J. Biomech., **48**(14), pp. 3796–3802.

[66] Solav, D., Rubin, M. B., Cereatti, A., Camomilla, V., and Wolf, A., 2016, “Bone Pose Estimation in the Presence of Soft Tissue Artifact Using Triangular Cosserat Point Elements,” Ann. Biomed. Eng., **44**(4), pp. 1181–1190.

[67] Ludewig, P. M., Phadke, V., Braman, J. P., Hassett, D. R., Cieminski, C. J., and Laprade,

R. F., 2009, “Motion of the Shoulder Complex during Multiplanar Humeral Elevation,” J. Bone Jt. Surg. - Ser. A, **91**(2), pp. 378–389.

[68] Standford University, 2020, “OpenSim::Body Class Reference” [Online]. Available: https://simtk.org/api_docs/opensim/api_docs/classOpenSim_1_1Body.html. Accessed on 17 May 2021.

[69] Standford University, 2017, “How Scaling Works” [Online]. Available: https://simtk-confluence.stanford.edu:8443/display/OpenSim/How+Scaling+Works. Accessed on 17 May 2021.

[70] Standford University, 2013, “How Inverse Kinematics Works” [Online]. Available: http://simtk-confluence.stanford.edu:8080/display/OpenSim/How+Inverse+Kinematics+Works. Accessed on 17 May 2021.

[71] Standford University, “How Forward Dynamics Works” [Online]. Available: https://simtk-confluence.stanford.edu:8443/display/OpenSim/How+Forward+Dynamics+Works. Accessed on 17 May 2021.

[72] Seth, A., Matias, R., Veloso, A. P., and Delp, S. L., 2016, “A Biomechanical Model of the Scapulothoracic Joint to Accurately Capture Scapular Kinematics during Shoulder Movements,” PLoS One, **11**(1), p. e0141020.

[73] Hicks, J. L., Uchida, T. K., Seth, A., Rajagopal, A., and Delp, S. L., 2015, “Is My Model Good Enough? Best Practices for Verification and Validation of Musculoskeletal Models and Simulations of Movement,” J. Biomech. Eng., **137**(2), p. 020905.

[74] Bourne, D. A., Choo, A. M., Regan, W. D., MacIntyre, D. L., and Oxland, T. R., 2011, “The Placement of Skin Surface Markers for Non-Invasive Measurement of Scapular Kinematics Affects Accuracy and Reliability,” Ann. Biomed. Eng., **39**(2), pp. 777–785.

[75] Jacquet, E., Chambert, J., Pauchot, J., and Sandoz, P., 2017, “Intra- and Inter-Individual Variability in the Mechanical Properties of the Human Skin from in Vivo Measurements on 20 Volunteers,” Ski. Res. Technol., **23**(4), pp. 491–499.

[76] Standford University, 2020, “OpenSim::EllipsoidJoint Class Reference” [Online]. Available: https://simtk.org/api_docs/opensim/api_docs/classOpenSim_1_1EllipsoidJoint.html. Accessed on 17 May 2021.

[77] Standford University, 2020, “OpenSim::WeldJoint Class Reference” [Online]. Available: https://simtk.org/api_docs/opensim/api_docs/classOpenSim_1_1WeldJoint.html. Accessed on 17 May 2021.

[78] Standford University, 2020, “OpenSim::InverseKinematicsSolver Class Reference” [Online]. Available: https://simtk.org/api_docs/opensim/api_docs/classOpenSim_1_1InverseKinematicsSolver.html#details. Accessed on 17 May 2021.

[79] Jędrzejewski-Szmek, Z., Abrahao, K. P., Jędrzejewska-Szmek, J., Lovinger, D. M., and Blackwell, K. T., 2018, “Parameter Optimization Using Covariance Matrix Adaptation—Evolutionary Strategy (CMA-ES), an Approach to Investigate Differences in Channel Properties Between Neuron Subtypes,” Front. Neuroinform., **12**, p. 47.

[80] Ozaki, Y., Yano, M., and Onishi, M., 2017, “Effective Hyperparameter Optimization

Using Nelder-Mead Method in Deep Learning," IPSJ Trans. Comput. Vis. Appl., **9**, p. 20.

Appendix A. Pseudocode of Key Algorithms

Algorithm 1 – Add float bodies, anchor bodies and markers to a model

```
Input: an OpenSim model, and a list of the number of float bodies to add to each body segment (Nf)
Output: the same model with float bodies and markers added
    Import OpenSim API and load model
    n = 0
    R = list of radii of each ellipsoid attached to each body segment
    For j from 1 to length(Nf) do:
        For i from 1 to Nf[j] do:
        n += 1
        O = list of three random numbers in the range [0 , 360] degrees
        Add body "floatbodyn" to model
        Add marker "floatmarkern" to model and attach it to the origin of floatbodyn
        Connect floatbodyn to body segment j via an ellipsoid joint "floatjointn" with orientation (O[0], O[1], O[2]) relative to body j and with radii R[j]
        End For
    End For
    AT = list of anchor body locations on thorax
```

```
AH = list of anchor body locations on humerus
For a from 1 to length(AT) do:
    Add body “anchorbodya” to model
    Add marker “anchormarkera” to model
    Weld anchorbodya to thorax
End For
For a from 1 to length(AH) do:
    b = a + length(AT)
    Add body “anchorbodyb” to model
    Add marker “anchormarkerb” to model
    Weld anchorbodyb to humerus
End For
Return the modified model
```

Algorithm 2 – Add repulsive forces between all float bodies

Input: model with float bodies added (output from Algorithm 1)

Output: the same model with repulsive forces added between each pair of float bodies

```
Import OpenSim API and load model
AllBodies = list of all float bodies in model
For body1 in AllBodies do:
    For body2 in AllBodies do:
        If body1 = body2:
            Continue
    End For
    Add repulsive force element between body1 and body2
End For
Return the modified model
```

Algorithm 3 – Create a new model without repulsive forces, and add springs and dampers

```
Input: modified model with repulsive forces added (output from Algorithm 2)
Output: new model without repulsive forces and with springs and dampers
    Use Algorithm 1 to create a new model
    Nj = list of all ellipsoid joints in Algorithm 1 model
    Run dynamic settling simulation of Algorithm 2 (input) model in the default pose
    For i from 1 to Nj do:
        Get 3 coordinates c1, c2 and c3 of joint i from Algorithm 2 model
        Set coordinates of joint i in Algorithm 1 model to c1, c2 and c3
    End For
    Nd = Number of float bodies in Algorithm 1 model
    Na = Number of anchor bodies in Algorithm 1 model
    For x from 1 to Nd do:
        Get 3 closest bodies to float body x
        Add springs and dampers using Eq. (1) where $k$ = 10 N/m, slack length is 10 cm and $c$ = 2.0 N·s/m
    End For
    For y from 1 to Na do:
        Get 2 closest bodies to anchor body y
        Add springs and dampers using Eq. (1) where $k$ = 10 N/m, slack length is 10 cm and $c$ = 2.0 N·s/m
    End For
    Return new model without repulsive forces and with springs and dampers
```

Algorithm 4 – Add spring–damper components between manually selected float bodies and anchor bodies

```
Input: model with float and anchor bodies
Output: model with spring–damper components between float and anchor bodies
    Import OpenSim API and load model
    P = list of lists of manually selected float body and anchor body pairs
    For i from 1 to length(P) do:
        Get bodies b1 and b2 from P[i]
        Get markers m1 and m2 corresponding to bodies b1 and b2
        L = distance between m1 and m2
        $L_{slack} = L \times 0.98$
        $F = k \times (L - L_{slack}) - cv$, where spring constant k = 10 N/m, damping coefficient c = 5.0 N·s/m, and $v = dL(t)/dt$
        Create force element to apply force F between bodies b1 and b2
    End For
    Return model with spring–damper components between float and anchor bodies
```

Algorithm 5 – Calculate joint angles given the locations of synthetic skin markers on the skinned upper-extremity model

```
Input: the skinned upper-extremity model (Figure 3.12B) and a list of thorax coordinate values over time (Tv)
Output: the value of each coordinate in the model at each point in time
    Import OpenSim API and load model
    Calculate center-of-float-box (COFB) trajectories in abduction motion (see Algorithm 6)
    Apply filter to COFB trajectories (see Algorithm 7) to simulate noise (optional)
    COFB = list of COFB trajectories over time
    CoordinateValues = [] # will contain optimized coordinate values
    For i from 1 to length(COFB) do:
        Set thorax coordinates to Tv[i]
        Run CMA-ES optimization (Algorithm 8)
        Set model coordinates to solution from optimizer
        Append solution to CoordinateValues
    End For
    Return CoordinateValues
```

Algorithm 6 – Calculate center-of-float-box (COFB) trajectories

```
Input: file containing thorax and shoulder coordinate values over time
Output: file containing COFB trajectories over time
    Import OpenSim API and load model
    Tv = list of thorax coordinate values
    Cv = list of shoulder coordinate values
    COFB = []
    For i from 1 to length(Cv) do:
        Set model’s thorax coordinates to Tv[i]
        Run InverseKinematicsSolver using Cv[i]
        Lock shoulder coordinates, and allow float bodies to settle
        Calculate center of each float box and append to COFB list
    End For
    Save COFB list to file
```

Algorithm 7 – Filter COFB trajectories

```
Input: file containing list of COFB trajectories (output from Algorithm 6)
Output: file containing list of filtered COFB trajectories
    Read COFB trajectory file
    For k from 1 to 3 do:
        Get COFB k
        For j from 1 to 3 do:
            $C_{kj}$ = list of positions of COFB k along axis j
            $F_{kj}$ = list $C_{kj}$ values with Savitzky-Golay filter applied
        End For
    End For
    Save $F_{kj}$ lists to file
```

Algorithm 8 – CMA-ES optimization of the skinned upper-extremity model's joint coordinates at one time step

```
Input: the skinned upper-extremity model in its default pose, and the location of experimental skin markers (COFB locations)
Output: model coordinate values at this time step
    Candidate solution = CMA-ES generated values for skeletal coordinates
    Run InverseKinematicsSolver using Candidate solution to ensure skeletal coordinates describe a feasible model pose
    Unlock (enable motion of) float bodies; lock (disable motion of) all other bodies
    It = 20.0 #duration of each interval for dynamic settling simulation (seconds)
    Mt = 200.0 #maximum permissible duration of dynamic settling simulation (seconds)
    Ta = 0.001 #maximum permissible float body acceleration at equilibrium
    t = 0.0 #current simulation time
    Bodyset = list of all float bodies in the model
    Maxa = infinity #will contain the maximum float body acceleration
    While t < Mt and maximum float body acceleration Maxa > Ta do:
        Run forward dynamic simulation for duration of It
        t = t + It
        Maxa = 0 #initialize
        For body in Bodyset do:
            Calculate acceleration of float body
            If float body acceleration > Maxa do:
                Maxa = float body acceleration
```

```
        End For
    End While
    J = distance between Model COFB and Experimental COFB
```